



AFRL-RX-WP-TR-2011-4122

EVALUATION OF “FUZZY FIBER” SENSORS FOR STRUCTURAL HEALTH MONITORING

Michael Bouchard, Khalid Lafdi, Norman Schehl, James Sebastian, and Yuhchae Yoon

University of Dayton Research Institute

NOVEMBER 2010

Final Report

Approved for public release; distribution unlimited.

See additional restrictions described on inside pages

STINFO COPY

**AIR FORCE RESEARCH LABORATORY
MATERIALS AND MANUFACTURING DIRECTORATE
WRIGHT-PATTERSON AIR FORCE BASE, OH 45433-7750
AIR FORCE MATERIEL COMMAND
UNITED STATES AIR FORCE**

NOTICE AND SIGNATURE PAGE

Using Government drawings, specifications, or other data included in this document for any purpose other than Government procurement does not in any way obligate the U.S. Government. The fact that the Government formulated or supplied the drawings, specifications, or other data does not license the holder or any other person or corporation; or convey any rights or permission to manufacture, use, or sell any patented invention that may relate to them.

This report was cleared for public release by the Air Force Research Laboratory, 88th Air Base Wing, Public Affairs Office (PAO) and is available to the general public, including foreign nationals. Copies may be obtained from the Defense Technical Information Center (DTIC) (<http://www.dtic.mil>).

AFRL-RX-WP-TR-2011-4122 HAS BEEN REVIEWED AND IS APPROVED FOR PUBLICATION IN ACCORDANCE WITH ASSIGNED DISTRIBUTION STATEMENT.

//Signature//

CHARLES F. BUYNAK, Project Engineer
Nondestructive Evaluation Branch
Metals, Ceramics, and NDE Division

//Signature//

STEPHAN M. RUSS, Chief
Nondestructive Evaluation Branch
Metals, Ceramics, and NDE Division

//Signature//

ROBERT T. MARSHALL, Deputy Chief
Metals, Ceramics, and NDE Division
Materials and Manufacturing Directorate

This report is published in the interest of scientific and technical information exchange, and its publication does not constitute the Government's approval or disapproval of its ideas or findings.

*Disseminated copies will show "//Signature//" stamped or typed above the signature blocks.

REPORT DOCUMENTATION PAGE				Form Approved OMB No. 0704-0188	
<p>The public reporting burden for this collection of information is estimated to average 1 hour per response, including the time for reviewing instructions, searching existing data sources, gathering and maintaining the data needed, and completing and reviewing the collection of information. Send comments regarding this burden estimate or any other aspect of this collection of information, including suggestions for reducing this burden, to Department of Defense, Washington Headquarters Services, Directorate for Information Operations and Reports (0704-0188), 1215 Jefferson Davis Highway, Suite 1204, Arlington, VA 22202-4302. Respondents should be aware that notwithstanding any other provision of law, no person shall be subject to any penalty for failing to comply with a collection of information if it does not display a currently valid OMB control number. PLEASE DO NOT RETURN YOUR FORM TO THE ABOVE ADDRESS.</p>					
1. REPORT DATE (DD-MM-YY) November 2010		2. REPORT TYPE Final		3. DATES COVERED (From - To) 11 May 2009 – 11 December 2010	
4. TITLE AND SUBTITLE EVALUATION OF “FUZZY FIBER” SENSORS FOR STRUCTURAL HEALTH MONITORING				5a. CONTRACT NUMBER FA8650-09-C-5234	
				5b. GRANT NUMBER	
				5c. PROGRAM ELEMENT NUMBER 62102F	
6. AUTHOR(S) Michael Bouchard, Khalid Lafdi, Norman Schehl, James Sabastian, and Yuhchae Yoon				5d. PROJECT NUMBER 4349	
				5e. TASK NUMBER 40	
				5f. WORK UNIT NUMBER LP106500	
7. PERFORMING ORGANIZATION NAME(S) AND ADDRESS(ES) University of Dayton Research Institute 300 College Park Dayton, OH 45469				8. PERFORMING ORGANIZATION REPORT NUMBER UDRI-TR-2011-14	
9. SPONSORING/MONITORING AGENCY NAME(S) AND ADDRESS(ES) Air Force Research Laboratory Materials and Manufacturing Directorate Wright-Patterson Air Force Base, OH 45433-7750 Air Force Materiel Command United States Air Force				10. SPONSORING/MONITORING AGENCY ACRONYM(S) AFRL/RXLP	
				11. SPONSORING/MONITORING AGENCY REPORT NUMBER(S) AFRL-RX-WP-TR-2011-4122	
12. DISTRIBUTION/AVAILABILITY STATEMENT Approved for public release; distribution unlimited.					
13. SUPPLEMENTARY NOTES PAO Case Number 88ABW-2011-1609; cleared 18 March 2011. Paper contains color. Also see AFRL-RX-WP-TR-2011-4095, AFRL-RX-WP-TR-2011-4096, and AFRL-RX-WP-TR-2011-4097					
14. ABSTRACT (Maximum 200 words) As advanced fiber composites are utilized more frequently in primary structural applications, there is a key challenge to enhance the performance and reliability while reducing maintenance. As a consequence, there is tremendous scientific and technical interest in the development of techniques for monitoring the health of composite structures where real-time sensing can provide information on the state of chemistry and micro-structural damage. In this study, it has been established that carbon nanotubes grown on carbon or glass fiber (nicknamed fuzzy fibers) can be utilized as electrical networks by transforming the insulating glass fiber to very conductive one. The fuzzy fiber was inserted into traditional composites during layup operations and then used as in situ sensors for detecting changes during oxidation of advanced fiber composites. In order to gain an insight toward the oxidation rate and durability of polymer composites, the integration of electrical resistance measurements through fuzzy fiber ends was used as function time. Fuzzy fiber grids built into composites enables tracking of oxidation rates between oxidation occurring at the core and skin of the composites. Using spectroscopy techniques, we were able to depict the oxidation mechanism and oxidation rate. During the degradation process, first oxygen adsorption took place and then, as the oxidation phenomena progressed, pits and cracks developed that led into structural properties. We identified a parameter that may be utilized as a quantitative measure of oxidation rate.					
15. SUBJECT TERMS structural health monitoring, composite structures, carbon nanotubes					
16. SECURITY CLASSIFICATION OF:			17. LIMITATION OF ABSTRACT: SAR	18. NUMBER OF PAGES 54	19a. NAME OF RESPONSIBLE PERSON (Monitor) Charles Buynak 19b. TELEPHONE NUMBER (Include Area Code) (937) 255-9807
a. REPORT Unclassified	b. ABSTRACT Unclassified	c. THIS PAGE Unclassified			

Table of Contents

<u>Section</u>	<u>Page</u>
List of Figures	iii
List of Tables	vi
Foreword	vii
1 INTRODUCTION 1	
1.1 Background	1
1.2 Technical Concept	2
1.3 Program Objectives and Scope	3
2 CORROSION SENSING	4
2.1 Objectives	4
2.2 Technical Approach	4
2.2.1 Sensor Concept	4
2.2.2 Deposition of Aluminum Alloys	4
2.2.3 Electrochemical OCP and EIS Measurements	4
2.3 Results and Discussion	5
2.3.1 Effect of CNT on the Carbon Tow	5
2.3.2 SEM/EDS Analysis of Aluminum Alloys on the Carbon Tow and Carbon-CNT	6
2.3.3 Effect of Aluminum Alloy Coatings on the Carbon Tow	7
2.3.4 Effect of Aluminum Alloy Coatings on the Carbon-CNT	9
2.3.5 Sensitivity of Aluminum Alloy Coatings on the Carbon Tow and Carbon-CNT	10
2.4 Summary and Recommendations	14
3 MECHANICAL SENSING	15
3.1 Objectives	15
3.2 Technical Approach	15
3.2.1 Sensor Development	15
3.2.2 Instrumentation Development	16
3.2.3 Fiber and Tow Tension Tests	17
3.2.4 Monocomposite Tension Tests	18
3.2.5 Composite Tests	19
3.2.5.1 Uniaxial and Orthotropic Coupon Tension Tests	20
3.2.5.2 Stress-Riser Tension Tests	22
3.2.5.3 Poisson and Off-Axis Tension Tests	24
3.3 Results and Discussion	27
3.3.1 Fiber and Tow Tension Tests	27
3.3.2 Monocomposite Tension Tests	28
3.3.3 Composite Tests	29
3.3.3.1 Uniaxial and Ortotropic Coupon Tension Tests	29
3.3.3.2 Stress-Riser Tension Tests	30
3.3.3.3 Poisson and Off-Axis Tension Tests	31

Table of Contents (Continued)

<u>Section</u>	<u>Page</u>
3.3.3.4 Thermal Sensitivity	33
4 OXIDATION SENSING	35
4.1 Use of the Fuzzy Fiber as an Oxidation Sensor	35
4.1.1 Objectives	35
4.1.2 CNT Growth on Glass Fibers	35
4.1.3 Oxidation of Bare Fibers	35
4.2 Use of CNT Fuzzy Fiber as an Oxidation Sensor in Epoxy-Based Composites	38
4.3 Use of CNT Fuzzy Fiber as an Oxidation Sensor in MVK14-Based Composites ...	41
4.4 Summary	42
4.5 Recommendation	42
5 REFERENCES	43

List of Figures

	<u>Page</u>
Figure 1 Carbon nanotube “fuzzy fibers” developed at UDRI	1
Figure 2 Cell configuration for the standard three-electrode measurement for the fuzzy fiber tow sensor in 3.5 wt% solution	5
Figure 3 OCPs of carbon tow and carbon tow-CNT in 3.5 wt% NaCl during 1-hr. immersion	5
Figure 4 EIS plots of (a) carbon tow and (b) carbon tow-CNT after 1-hr. immersion in 3.5 wt% NaCl.....	6
Figure 5 Typical EDS spectra of a carbon tow-CNT, carbon tow-CNT-AA2024, and carbon tow-CNT-AA-7075	7
Figure 6 SEM images of (a) carbon tow-CNT, (b) carbon tow-CNT-AA2024, and (c) carbon tow-CNT-AA7075	8
Figure 7 OCPs of carbon tow with AA2024 and AA7075 coatings in 3.5 wt% NaCl during 1-hr. immersion	9
Figure 8 EIS plots of (a) impedance and (b) phase angle of carbon tow, carbon tow-CNT-AA2024, and carbon tow-CNT-AA7075 after 1-hr. immersion in 3.5 wt% NaCl.....	9
Figure 9 OCPs of carbon tow-CNT with AA2024 and AA7075 coatings in 3.5 wt% NaCl during 1-hr. immersion	10
Figure 10 EIS plots of (a) impedance and (b) phase angle of carbon tow-CNT, carbon tow-CNT-AA2024, and carbon tow-CNT-AA7075 after 1-hr. immersion in 3.5 wt% NaCl.....	10
Figure 11 EIS plots of (a) impedance and (b) phase angle of carbon tow and carbon tow-CNT after 1-hr. and 24-hr. immersion in 3.5 wt% NaCl	11
Figure 12 EIS plots of (a) impedance and (b) phase angle of carbon tow-CNT-AA2024 during 72-hr. immersion in 3.5 wt% NaCl	11
Figure 13 EIS plots of (a) impedance and (b) phase angle of carbon tow-CNT-AA7075 during 72-hr. immersion in 3.5 wt% NaCl	12
Figure 14 OCP and impedance plots of (a) carbon tow-CNT-AA2024 and (b) carbon tow-CNT-AA7075 during 72-hr. immersion in 3.5 wt% NaCl	12
Figure 15 EIS plots of (a) impedance and (b) phase angle of carbon tow-CNT-AA2024 during 24-hr. immersion in 3.5 wt% NaCl	13
Figure 16 EIS plots of (a) impedance and (b) phase angle of carbon tow-CNT-AA7075 during 24-hr. immersion in 3.5 wt% NaCl	13
Figure 17 OCP and impedance plots of (a) carbon tow-CNT-AA2024 and (b) carbon tow-CNT-AA7075 during 48-hr. immersion in 3.5 wt% NaCl	13
Figure 18 Fuzzy-fiber sensors enclosed in electrical isolation e-glass veil	16
Figure 19 Initial conductive epoxy bond between fiber tow and instrumentation lead	17
Figure 20 Radiograph of refined conductive epoxy bond between wire tow and instrumentation lead.....	17
Figure 21 Post-test fuzzy fiber tow	18
Figure 22 Epoxy matrix monocomposite with imbedded fiber tow.....	18
Figure 23 Testing of monocomposite in a hydraulic test system with an extensometer to measure strain	19
Figure 24 Composite panel layup with embedded sensors	19

List of Figures (Continued)

	<u>Page</u>
Figure 25 Panels in preparation state for autoclave cure.....	19
Figure 26 Use of an abrasive saw to machine specimens from panels	19
Figure 27 Composite panel with embedded strain sensors oriented for straight- sided specimens	20
Figure 28 Straight-sided specimen for strain sensitivity measurements	21
Figure 29 Schematic of straight-sided specimen with imbedded sensor.....	21
Figure 30 Test system consisting of an MTS 458 analog controller and 100kN servoactuator in a vertical load frame	21
Figure 31 Sensors positioned during composite panel fabrication.....	23
Figure 32 Fabricated panel with embedded sensors.....	23
Figure 33 Open-hole stress-concentration specimen prepared for testing	23
Figure 34 Schematic representative of the sensor locations.....	23
Figure 35 Insertion of fuzzy fiber sensors in the transverse orientation	24
Figure 36 Insertion of fuzzy fiber sensors in the longitudinal orientation	24
Figure 37 Final form of Poisson's specimen.....	25
Figure 38 Schematic with sensor locations	25
Figure 39 Final specimen configuration with longitudinal and transverse sensors installed in the materials test system.....	26
Figure 40 Sensor-orientation specimen	26
Figure 41 Four-fiber data	27
Figure 42 Low-CNT doping initial data.....	28
Figure 43 High-CNT doping initial data	28
Figure 44 Initial low-doping monocomposite data	28
Figure 45 Initial high-doping monocomposite data	28
Figure 46 Monocomposite intermediate test series	29
Figure 47 Final format monocomposite strain data.....	29
Figure 48 Uniaxial specimen strain data	30
Figure 49 Orthotropic specimen strain data	30
Figure 50 Tension test sensitivity.....	30
Figure 51 Stress-riser specimen data.....	31
Figure 52 Sensor response in uniaxial composite loaded along its axis	32
Figure 53 Typical off-axis sensor response.....	33
Figure 54 Off-axis sensitivity data	33
Figure 55 Drift during slow tension test.....	33
Figure 56 Minimal drift during fast tension test.....	33
Figure 57 Fuzzy fiber sensor thermal response.....	34
Figure 58 Fuzzy fiber with less-dense CNT.....	35
Figure 59 Fuzzy fiber with very dense and longer CNT	35
Figure 60 Resistance measurement of fuzzy fibers with 2- and 5-min. growth resident time.....	36
Figure 61 Weight loss and resistance measurement of fuzzy fibers with 2- and 5-min. growth resident time	36
Figure 62 Resistance measurement setup.....	36
Figure 63 Resistance measurement of bare fuzzy fibers at average temperature	37
Figure 64 Oxidation rate measurement based on Figure 63.....	37

List of Figures (Continued)

	<u>Page</u>
Figure 65 Resistance measurement of bare fuzzy fibers (second run).....	37
Figure 66 Oxidation rate measurement based on Figure 65.....	37
Figure 67 XPS of a sample oxidized for 30 min.	38
Figure 68 XPS of a sample oxidized for 5 hours	38
Figure 69 XPS zoom of the carbon oxygen picture for 5 hours oxidation's sample	38
Figure 70 Expanded view of oxidation sensor composite.....	38
Figure 71 Sketch of test setup	39
Figure 72 Resistance data for sensors inside of heater.....	39
Figure 73 Data for sensors outside of heater	39
Figure 74 Oxidation rates for internal sensor inside heater.....	40
Figure 75 Oxidation rates for surface sensor inside heater	40
Figure 76 Data for epoxy-based composites (sensors outside of heater)	40
Figure 77 Oxidation rate comparison between external and internal sensor	40
Figure 78 Data for MVK14-based composites.....	41
Figure 79 Oxidation rates for surface sensor for MVK14-based composites	41
Figure 80 Pristine sample before oxidation.....	41
Figure 81 Pristine sample before oxidation.....	41
Figure 82 Sample after oxidation showing development of pits and cracks	41

List of Tables

Table 1	Straight-Sided Specimen Parameters	22
Table 2	Open-Hole Stress-Concentration Specimen Parameters	24
Table 3	Poisson Ratio Specimen Parameters	25
Table 4	XPS Results of Oxidized Samples Showing the Oxygen/Carbon Ratio	38

Foreword

The effort reported herein was conducted by the Structural Integrity Division of the University of Dayton Research Institute (UDRI) during the time period 11 May 2009 through 11 February 2011. The work was conducted under Air Force Contract FA8650-09-C-5324, with Air Force technical management provided by Mr. Charles Buynak, AFRL/RXLP. UDRI program management was provided by Mr. Michael Bouchard, with Dr. Khalid Lafdi serving as Principal Investigator. Dr. Yuhchae Yoon directed the corrosion sensor research, Mr. James Sebastian and Mr. Norman Schehl directed the mechanical sensor research, and Dr. Lafdi directed the oxidation sensor research. The authors gratefully acknowledge the contributions of the following individuals: Mr. Matt Boehle (UDRI) for sensor fabrication and star sample fabrication; Mr. Ronald Trejo (UDRI) for composite panel and sample fabrication; AFRL/RXBC for providing materials and access to manufacturing facilities to fabricate composite panels and samples; Dr. Thomas Whitney (UDRI) for consulting regarding coupon selection; Dr. Geoffrey Frank (UDRI) for supporting composite laminate analysis; and Ms. Andrea Snell (UDRI) for preparing the final report manuscript.

Section 1

Introduction

Structural Health Monitoring (SHM) seeks to provide ongoing monitoring of a structure's integrity, minimizing the need for programmed inspections and allowing maintenance to be need-driven, rather than usage-driven. Current SHM approaches often use strain gages, accelerometers and, more recently, piezoelectric sensors. These provide "point" measurements of engineering information, therefore, they must be placed at or near critical regions of interest in order to detect damage. Should damage occur at other unanticipated regions, it may go undetected. Methods have been devised to use the sensors in a network to "triangulate" readings/locations of interest. This is especially true for piezoelectric sensors, which provide an actuation, as well as a sensing function [1,2]. In the end, though, all of these schemes rely on point-wise measurements and have the potential of not detecting damage. The goal of the program documented herein was to demonstrate a novel, multi-modal, nanomaterials-based sensor technology that can provide wide-area detection of damage.

1.1 Background

One approach to wide-area damage detection is to harness the ability of certain classes of materials to provide a self-diagnosing function. Schulte's group has reported that measuring changes in electrical resistance of carbon fiber-reinforced plastic composites during tensile and fatigue loading can be used as an NDE technique [3,4]. The same idea was used to detect the water leakage in reinforced concrete, in which the cement mortar conductivity decreased with decreasing water content and leakage [5]. The proposed effort seeks to harness the inherent conductivity of carbon nanotubes (CNTs) to provide for in-situ sensing of structural damage [6].

CNTs are made of graphene sheets of hexagonal structure rolled up into a nanoscale tube. For single-walled carbon nanotubes (SWCNTs), only one graphene sheet is used to form the tube, while additional graphene tubes around the core of an SWCNT lead to multi-walled carbon nanotubes (MWCNTs). These CNTs have diameters in a range between one to tens of nanometers, with both their ends normally capped by fullerene-like structures. The unique structure of CNTs brings the materials some outstanding properties that make them possible to find applications in various areas of materials, including the development of a new generation of sensors. Figure 1 shows an SEM image of CNT on carbon fibers. Due to their appearance, we refer to such CNT-coated fibers as "fuzzy fibers."

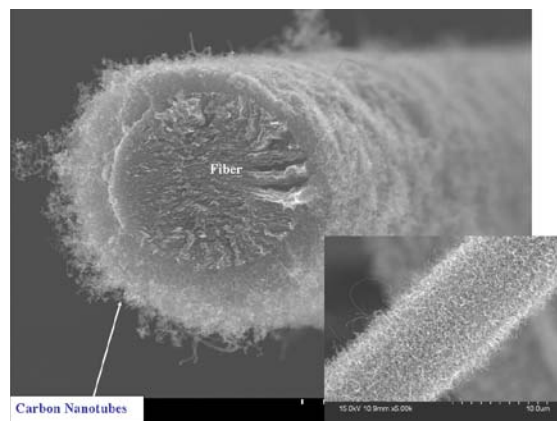


Figure 1. Carbon nanotube "fuzzy fibers" developed at UDRI.

Electrochemical sensors and biosensors are, possibly, among the most intensively studied applications for CNTs. Carbon nanotubes are promising materials for detecting chemicals and biochemicals due to several intriguing properties, including their outstanding ability to mediate fast electron-transfer kinetics for a wide range of electroactive species and large length-to-diameter aspect ratios that provide high surface area. This large surface area offers an opportunity for depositing external materials or performing surface functionalization that may bring or enhance activity of electrodes [6-9]. Factors that make CNTs impressive for electroanalytical applications

include the ability of this nanomaterial to promote electron transfer in electrochemical reactions, high electrocatalytic activities towards chemicals and biomolecular species, and anti-fouling capability of the electrode surfaces [10-13].

The CNT's large surface area gives significant gas-molecular adsorption capacity. The adsorption of electron withdrawing or donating gas molecules on CNTs can cause charge transfer between the nanotubes and molecules [14]. This charge transfer can lead to changes in the electrical conductance of the nanotubes. The direct change in their electrical properties in response to the interaction with probed molecules forms the basis for gas molecular sensors.

Coatings or modification of the nanotubes with certain metals (*e.g.*, Pd nanoparticles [15], etc.), metal oxides (*e.g.*, SnO₂ nanoparticles [16], etc.), polymers (*e.g.*, polyethyleneimine [17] and poly-(*m*-aminobenzene sulfonic acid [18], etc.) have been demonstrated to impart selectivity to the sensors for certain gases and vapors, as well as to allow for detection of molecular species at low concentrations. Functionlization of CNTs may also give biomolecular recognition that may lead to biosensors in addition to the gas and vapor molecular sensors based on change of electrical conduction [19]. In addition to coating or surface modification, doping CNTs with certain elements (*e.g.*, nitrogen doping during CNT synthesis) can enhance sensitivity and selectivity to certain gas molecular species.

Strain and bending of CNTs may cause reproducible changes in their conductance, making it possible to construct electromechanical sensors [20,21]. The piezoresistance properties of CNTs in polymeric composites are being investigated for smart structure applications [22-23].

There are a number of other CNT sensors under study that may have working principles completely or partially different from the above sensors. For example, based on the change of mechanical resonant frequency of CNTs due to variation of temperature, pressure, mass, and strain, the corresponding thermal sensors, pressure sensors, mass sensors, and strain sensors were suggested [24]. Based on the fact that there are shifts of specific peaks in the Raman spectrum of CNTs dispersed in polymeric composites under stress-strain or pressure, CNTs may be used for sensing stress and pressure [25].

1.2 Technical Concept

UDRI has developed processes to grow nanotubes onto both carbon and fiberglass composite tow fibers and weaves to improve thermal conductivity and other properties for a variety of applications, including friction (braking), high-performance carbon-carbon composites, EMI shielding, lightning strike, energy storage, thermal management, bio-implants, and bone regeneration (pending patent #60/800,944: Method of Growing Carbon Nanotubes and Nanofibers and Whiskers on Carbon Substrates). Work has been completed in adapting fuzzy fibers to individual fibers or tows, 6" carbon and glass fabrics (pending patent #60/800,944: Method of Growing Carbon Nanotubes and Nanofibers and Whiskers on Carbon Substrates).

Based on the body of work described above, UDRI believed that fuzzy fibers may be integrated into practical aircraft structures to detect various modes of damage. In this approach, the sensors are an integral part of the composite structure and may exhibit several significant attributes:

- *Manufacturability* – They can be integrated into a composite structure in a variety of ways, including as separate add-ins on or between plies, included in the tow, or woven into the fabric or preform.

- *Wide-area detection* – The fact that they can be integrated into practical composite forms is an important enabler to wide-area sensing and monitoring of damage in composite and hybrid structures.
- *Material compatibility* – They are formulated of the same material as the composite fibers (carbon), ensuring material compatibility.
- *Multiple sensing modalities* – In addition to detecting changes in strain, they also can detect chemical presence. Thus, the sensor can be used, not only to detect mechanical damage, but also corrosion of metal structures. Outside the focus of the proposed program, but also of relevance, is that fuzzy fibers can be optimized to dissipate (conduct) heat in high-temperature applications. Changes in heat conduction can be sensed, monitored, and used as an indicator of damage (*i.e.*, impact damage on hot leading-edge structures). They also may be able to detect oxidation of a composite structure.
- *Reduced part count* – Since the sensor is a continuous fiber, it can act as its own “lead wire”. By thoughtful arrangement of the fiber, as well as planning of the data acquisition and processing, terminals or bus bars can be positioned at a few logical locations on the structure, yet damage can be located to its specific site of occurrence. A “rat’s nest” of wires and electrical connectors is minimized.
- *Transition* – Scale-up of fuzzy fibers, possibly with multiple sensing modalities, into tow spools should be straightforward, enabling routine use in the manufacturing of composite structures.

1.3 Program Objectives and Scope

The overall objective of this program was to develop and characterize carbon nanotube, fuzzy fiber tows with sensing functions for corrosion, mechanical strain, and oxidation. The effort focused on individual sensor development, sensor characterization, incorporation into structural materials, and explorations using standard corrosion, mechanical, and oxidation test methods.

The report is organized by, and documents the research and results for, each of the three sensing modes: corrosion, mechanical elongation, and oxidation.

Section 2

Corrosion Sensing

2.1 Objectives

The purpose of the corrosion sensing research was to investigate the use of fuzzy fiber tows as corrosion sensors. The research focused on development of a corrosion sensor and, then, the characterization of the sensor using industry-standard, open-circuit potential (OCP) and electrochemical impedance spectra (EIS) measurement techniques.

2.2 Technical Approach

2.2.1 Sensor Concept

The working principle for the corrosion sensor was to couple the corrosion of aircraft aluminum alloys with the conductivity of nanomaterials, that is, aluminum corrosion would be detected as a change in sensor electrical response. The sensor concept to accomplish this was as follows: carbon nanotubes (CNT) were grown on a graphite tow to provide tailorable, electrical responsiveness. The CNTs, in turn, were coated with an aluminum alloy. The high surface area provided by the CNT “carpet” on the tow was expected to provide considerable bonding area for the aluminum alloy coating, resulting in increased sensitivity to electrical response. In operation, the alloy would match that of the structure to which it would be applied and the sensor, thus, would serve as a proxy for the corrosion in the actual structure.

2.2.2 Deposition of Aluminum Alloys

Aluminum alloys were deposited on both carbon tows and carbon tows with CNT. The former provided a baseline to which the latter’s response could be compared. Sputter deposition was used to apply the coatings of aluminum alloys on the carbon tow and carbon-CNT. This was accomplished using alloy AA2024 and AA7075 targets which were 7.62 mm in diameter and 0.5-1 mm in thickness. The sputtered coatings were obtained using a DC/RF sputtering unit (Denton Vacuum: The Denton Discovery[®] 18 System). The sputtering chamber was evacuated and filled with Ar. The base operating pressure was also about 2×10^{-7} Torr. The accelerating voltage and ion current were maintained about 0.5 kV and 0.65 A. To achieve a uniform thickness and composition of thin film coating, the substrate holder was rotated during operation. To monitor the coating thickness, the thin film coatings were also deposited on quartz crystal at room temperature with Ar⁺ ions. The deposition rate was approximately 0.067 nm/s. After deposition, the compositions and morphology of the thin film coatings were confirmed using energy-dispersive spectroscopy (EDS, Genesis 2000) and scanning electron microscopy (SEM, Zeiss EVO-500XVP). The nominal compositions of the AA2024 and AA7075 thin film coating were 94.7 wt.%Al-5.3 wt.%Cu and 91.6 wt.%Al-6.6 wt.%Zn-1.8 wt.%Mg, respectively.

2.2.3 Electrochemical OCP and EIS Measurements

The electrochemical experiments were performed in a three-electrode cell (Figure 2). A saturated calomel electrode (SCE) and a platinum mesh were used as reference and auxiliary electrodes, respectively. Three electrodes were used for characterization of electrochemical behavior of the carbon tow and carbon tow-CNT with the aluminum alloy coatings in terms of OCP/EIS. OCP was continuously measured on the specimens. Electrochemical impedance spectroscopy measurements (Gamry Reference 600 Potentiostat/Galvanostat/ZRA) were conducted with 15 mV amplitude from 10^5 to 10^{-2} Hz at OCP. The electrolyte of the 3.5 wt% NaCl solution was prepared with de-

ionized water ($18 \text{ M}\Omega\text{-cm}$). The full-frequency EIS scans were made to determine the impedance behavior of the specimen as a function of time. Since the limiting impedance at low frequencies is the sum of the solution resistance (R_s) and the polarization resistance (R_p), the absolute impedance measured at 10 mHz was used to represent the total impedance of the specimen for comparison among carbon tow and carbon tow-CNT with/without the aluminum alloy coatings in 3.5 wt% NaCl solution [26].

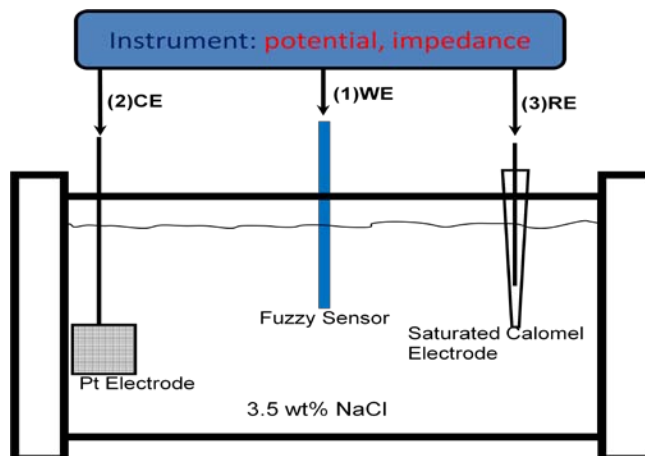


Figure 2. Cell configuration for the standard three-electrode measurement for the fuzzy fiber tow sensor in 3.5 wt% NaCl solution. (1) working electrode, (2) counter electrode, and (3) reference electrode.

2.3 Results and Discussion

2.3.1 Effect of CNT on the Carbon Tow

The effect of the CNT on the carbon tows were observed through experiments in 3.5 wt% NaCl solution. Figure 3 shows the evolution of the OCP of carbon tows and carbon tows with CNT. The OCP variations were characterized by a decrease within 600 s followed by stabilization. The OCPs of the carbon tows and carbon tows with CNT in the stable region were -450 and $-180 \text{ mV}_{\text{SCE}}$, respectively. The enhancement of OCP with CNT to more-positive values is reported in the literature [27].

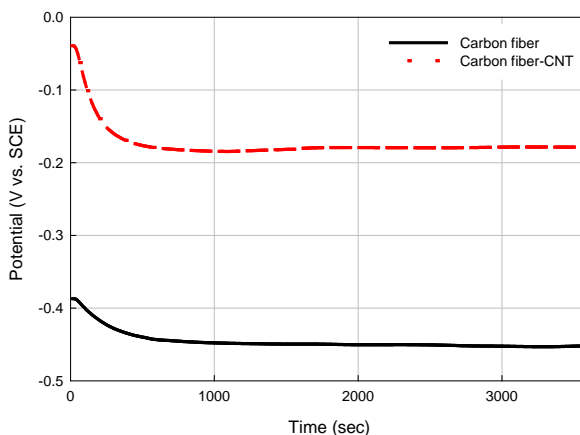


Figure 3. OCPs of carbon tow and carbon tow-CNT in 3.5 wt% NaCl during 1 hr. immersion.

Figure 4 shows the EIS plots of $\log |\text{impedance}|$ and phase angle (θ) of carbon tows and carbon tows with CNT after 1-hour immersion in 3.5 wt% NaCl. The impedance behavior is expressed in terms of real and imaginary components. At very-high frequency, the imaginary component disappears, leaving only the solution resistance. At very-low frequency, the imaginary component again disappears, leaving a sum of the solution resistance and the polarization resistance. Especially at the intermediate frequencies of Figure 4(a), the capacitance behaviors are observed with maximum phase angle. The polarization resistance is inversely proportional to the corrosion rate, which can be calculated from the impedance values at low and high frequencies. The polarization resistance is close to the impedance value at low frequency since the impedance value of the high frequency is much lower than that of the low frequency. Therefore, polarization resistances of the carbon tows and carbon tows with CNT were about 800 and 30 Ω , respectively. It is noted that this decrease in EIS values with CNT indicates that the conductivity of the carbon tows with CNT is much greater than that of carbon tows alone.

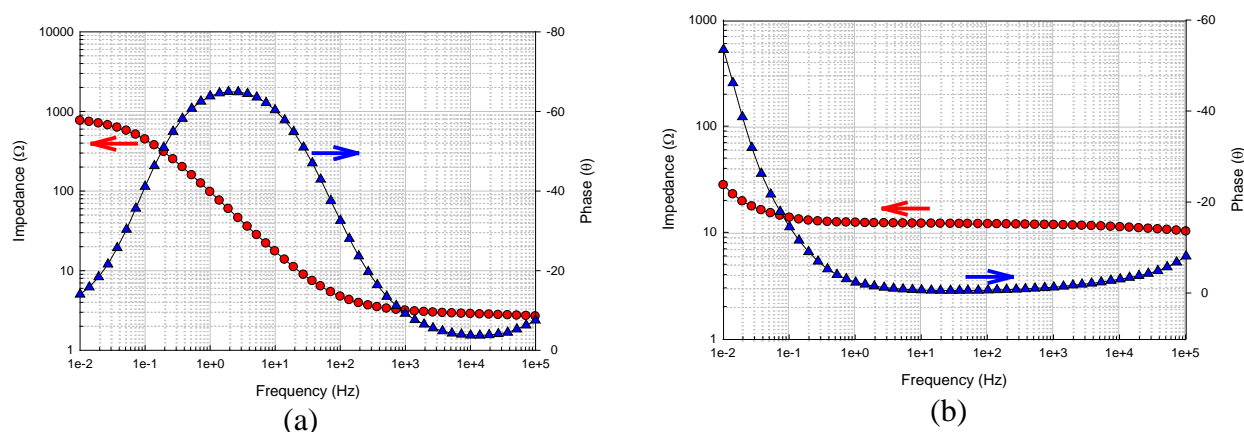


Figure 4. EIS plots of (a) carbon tow and (b) carbon tow-CNT after 1hr immersion in 3.5 wt% NaCl.

2.3.2 SEM/EDS Analysis of Aluminum Alloys on the Carbon Tow and Carbon-CNT

Figure 5 shows EDS spectra collected after aluminum alloy 2024 and 7075 sputtering coating on the carbon-CNT. The EDS spectra of the carbon-CNT, carbon-CNT-AA2024, and carbon-CNT-AA7075 were 90 wt% C- 10 wt% O, 94.7 wt% Al-5.3 wt% Cu, and 91.6 wt% Al-6.6 wt% Zn-1.5 wt% Mg, respectively. The EDS spectra indicate the chemical elements of the aluminum alloy coatings on the carbon-CNT, as well as carbon tow alone, were close to the nominal composition of the aluminum alloys. The aluminum coatings fully covered the carbon tow and carbon-CNT.

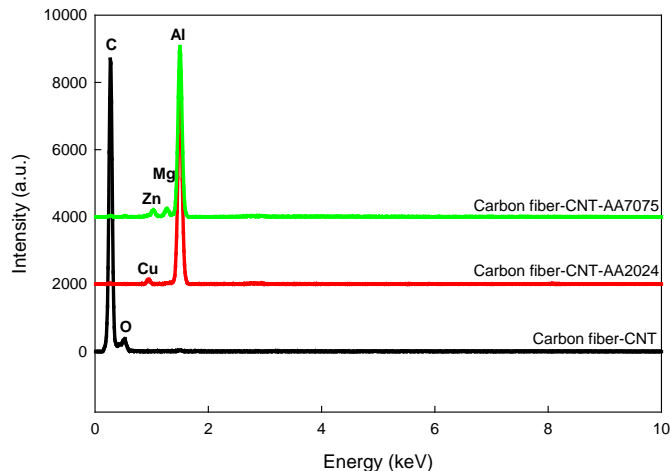


Figure 5. Typical EDS spectra of a carbon tow-CNT, carbon tow-CNT-AA2024, and carbon tow-CNT-AA7075. The intensities are offset vertically by 2000.

SEM images reveal the typical morphology of the aluminum alloys coated on the carbon-CNT tows in Figure 6. Both have chunky particles up to 10 μm on the carbon-CNT tows. Under the same sputtering conditions, there was no significant difference between the AA2024 and AA7075 coatings on the carbon tow. However, the diameter of the carbon tow with AA7075 is slightly larger than that of AA2024, which might indicate the deposition rate of AA7075 was faster than AA2024.

2.3.3 Effect of Aluminum Alloy Coatings on the Carbon Tow

Figure 7 shows the variations of each OCP versus time in 3.5 wt% NaCl. As can be seen, the aluminum coatings decreased the OCPs to a more-negative potential direction compared to carbon tow alone. With time, OCPs of both aluminum alloy-coated carbon tows were stabilized. The OCP of AA2024-coated carbon tow was stabilized from -770 mV_{SCE} to -700 mV_{SCE} during 1-hour immersion, while the OCP of AA7075-coated carbon tow exhibited a more-significant increase from -1000 mV_{SCE} to -780 mV_{SCE} . In these experiments, the OCP behaviors of the AA2024- and AA7075-coated carbon tows were similar to the bulk aluminum alloys.

Figure 8 shows the EIS plots of (a) $\log |\text{impedance}|$ and (b) phase angle (θ) as a function of a frequency in carbon-CNT with AA2024 and AA7075 coatings after 1-hour immersion in 3.5 wt% NaCl. The EIS behaviors of the aluminum alloy coatings on the carbon tows were slightly different than the carbon tow alone. Especially at high-frequency ranges, the impedance values decreased and the phase angles changed to 20 degrees, which suggests that there might be an inductive behavior, such as adsorption on the aluminum alloy coatings of the carbon tows.

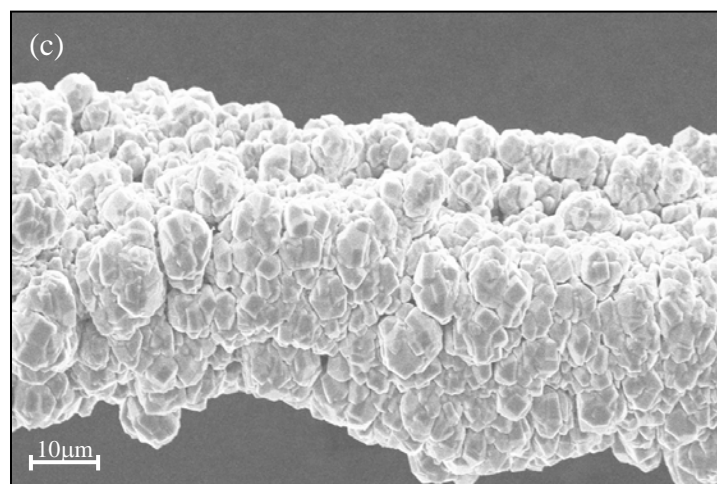
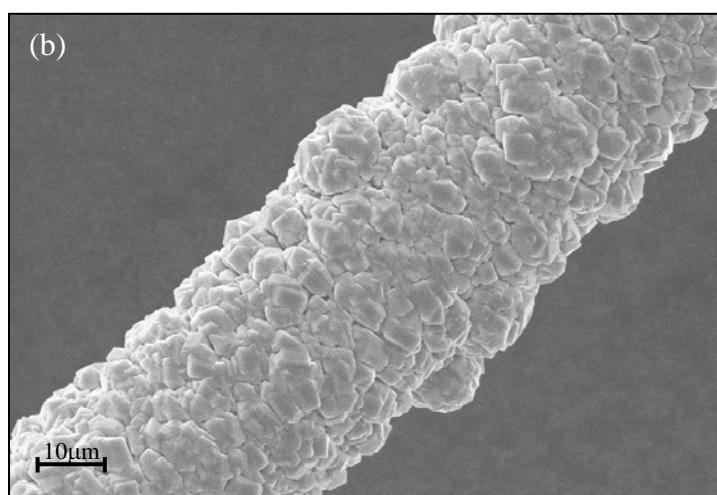
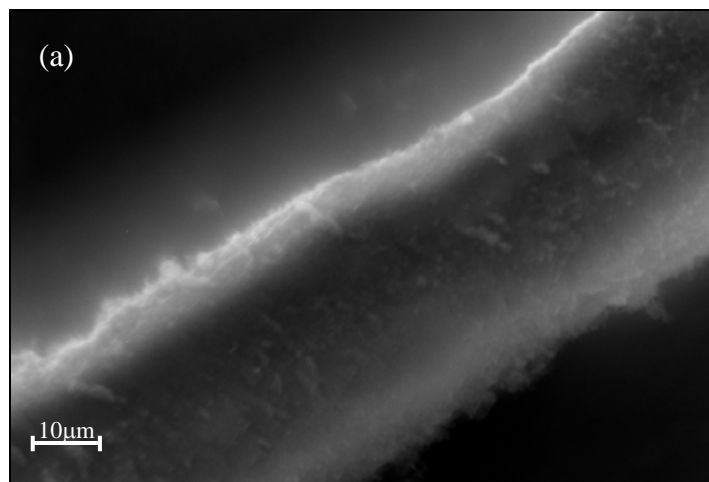


Figure 6. SEM images of (a) carbon tow-CNT, (b) carbon tow-CNT-AA2024, and (c) carbon tow-CNT-AA7075.

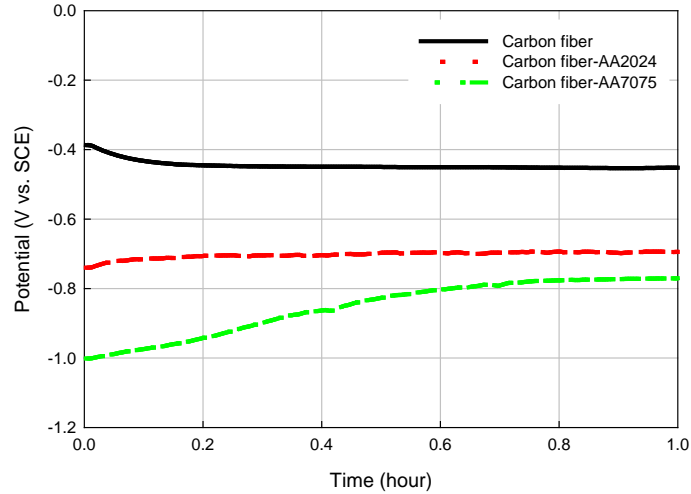


Figure 7. OCPs of carbon tow with AA2024 and AA7075 coatings in 3.5 wt% NaCl during 1-hr. immersion.

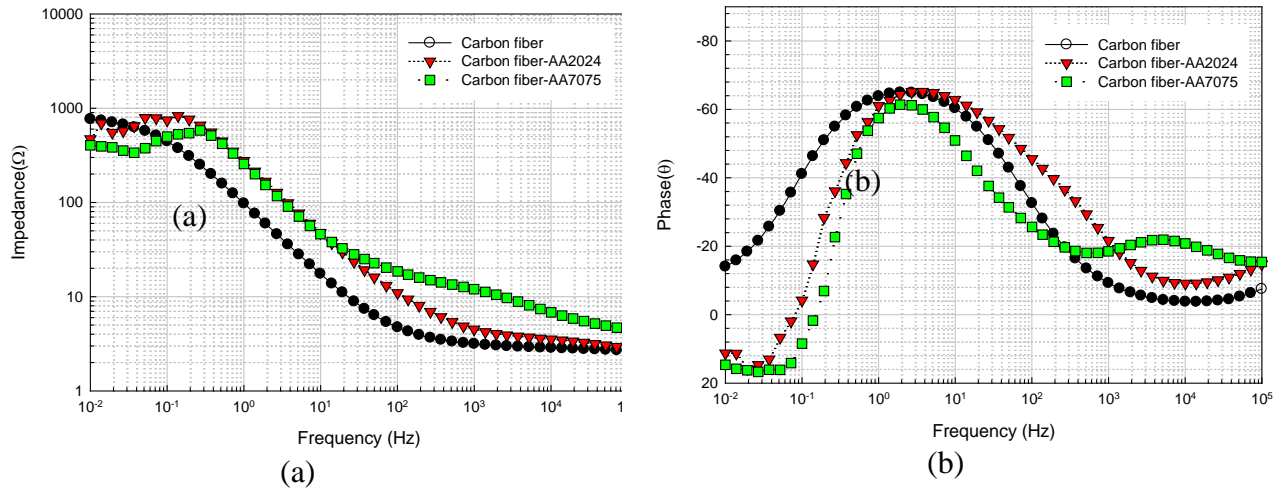


Figure 8. EIS plots of (a) impedance and (b) phase angle of carbon tow, carbon tow-CNT-AA2024, and carbon tow-CNT-AA7075 after 1-hr. immersion in 3.5 wt% NaCl.

2.3.4 Effect of Aluminum Alloy Coatings on the Carbon-CNT

The OCPs of AA2024 and AA7075 coatings on the carbon-CNT in 3.5 wt% NaCl are seen in Figure 9. The OCP behaviors were similar to those of the aluminum alloy coatings on the carbon tow alone in Figure 7. The OCP values of the aluminum alloys coatings on the carbon tow-CNT were slightly higher than those on the carbon tow alone. The EIS behaviors of the aluminum alloy-coated carbon tow-CNT were slightly different from that of tow-CNT without aluminum coating after 1-hour immersion in 3.5 wt% NaCl (Figure 10). The impedance values of the aluminum alloy-coated carbon tow-CNT at high-frequency regions were about 60 Ω , which were higher than the value of the tow-CNT alone (20 Ω). This result indicates that the conductivity decreased with aluminum alloy coatings on the tow-CNT.

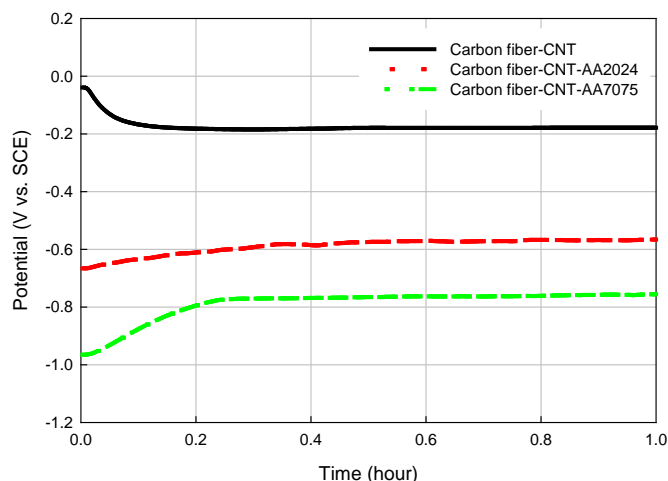


Figure 9. OCPs of carbon tow-CNT with AA2024 and AA7075 coatings in 3.5 wt% NaCl during 1-hr. immersion.

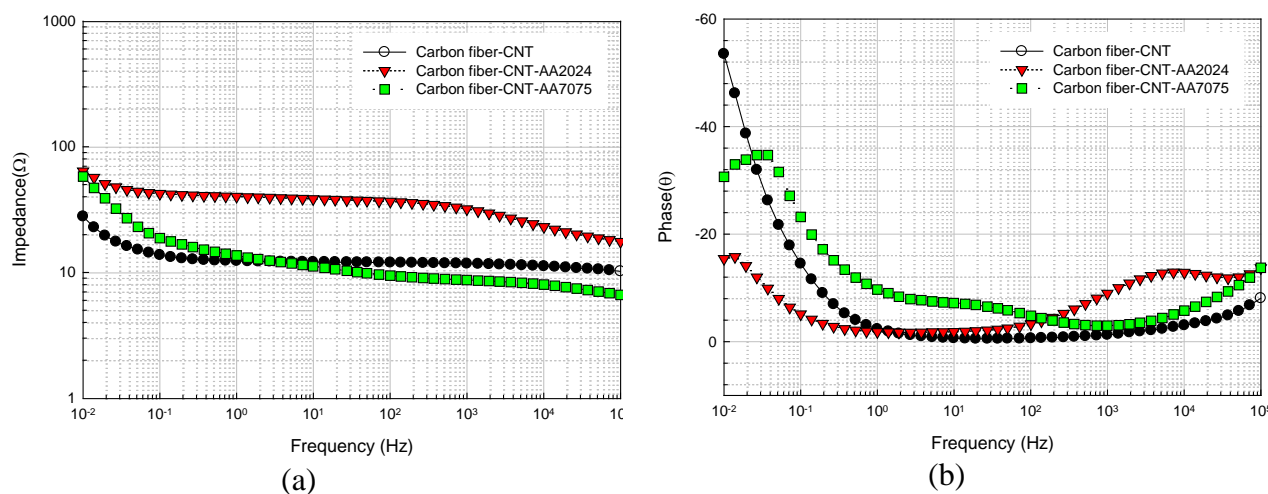


Figure 10. EIS plots of (a) impedance and (b) phase angle of carbon tow-CNT, carbon tow-CNT-AA2024, and carbon tow-CNT-AA7075 after 1-hr. immersion in 3.5 wt% NaCl.

2.3.5 Sensitivity of Aluminum Alloy Coatings on the Carbon Tow and Carbon-CNT

The sensitivity of impedance evolution with aluminum alloy coatings on the carbon tow and carbon tow-CNT in 3.5 wt% NaCl was monitored. Figure 11 shows the difference in EIS behaviors between 1-hour and 24-hour immersion for both carbon tow and the carbon tow-CNT. As can be seen, there is no effect of immersion time on the EIS behaviors. After application of the aluminum alloy coatings on the carbon tow and carbon-CNT, there was time-dependent sensitivity.

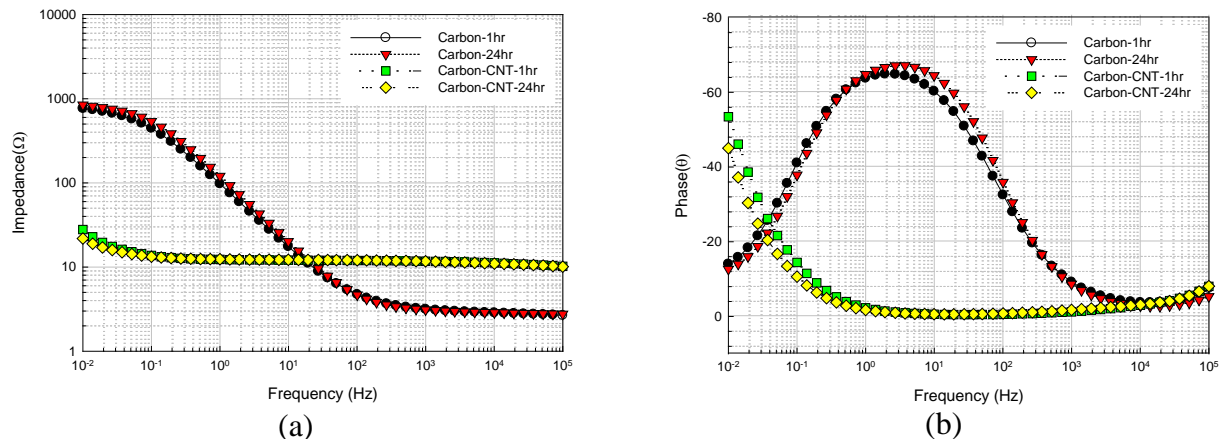


Figure 11. EIS plots of (a) impedance and (b) phase angle of carbon tow and carbon tow-CNT after 1-hr. and 24-hr. immersion in 3.5 wt% NaCl.

Figures 12 and 13 show the EIS behaviors of the carbon tow with AA2024 and AA7075 up to 72 hours immersion in 3.5 wt% NaCl. As immersion time goes on, the impedance value increased and the phase angle also changed to the negative direction. Figure 14 summarizes the OCP and impedance values of the carbon tows with AA2024 and AA7075 in 72-hour immersion in 3.5 wt% NaCl solution. OCPs were continuously monitored and averaged every hour; EIS was also measured every hour. As can be seen, the changes of OCP and impedance values were almost alike. The OCP values at early immersion time on the carbon-AA2024 and carbon-AA7075 were around -700 mV_{SCE} and -850 mV_{SCE}, respectively, and then both OCP values changed to -200 mV_{SCE} with increasing immersion time, which is similar to the OCP values of the carbon tow in Figure 3. In addition, the impedance values also significantly increased from $10^2 \Omega$ to $10^4 \Omega$. The initial impedance values were close to those of the aluminum alloys, later reaching the impedance value of the carbon tow in Figure 2. These results suggest that the aluminum alloy coatings on the carbon tow in the 3.5 wt% NaCl experienced metal dissolution and the values of the OCPs and initial impedances, which reflected the presence of aluminum alloys, changed to those values of the carbon tow. Those transitions were monitored around 40 hours of immersion. Note that the carbon-AA2024 exhibited more-rapid change than carbon-AA7075.

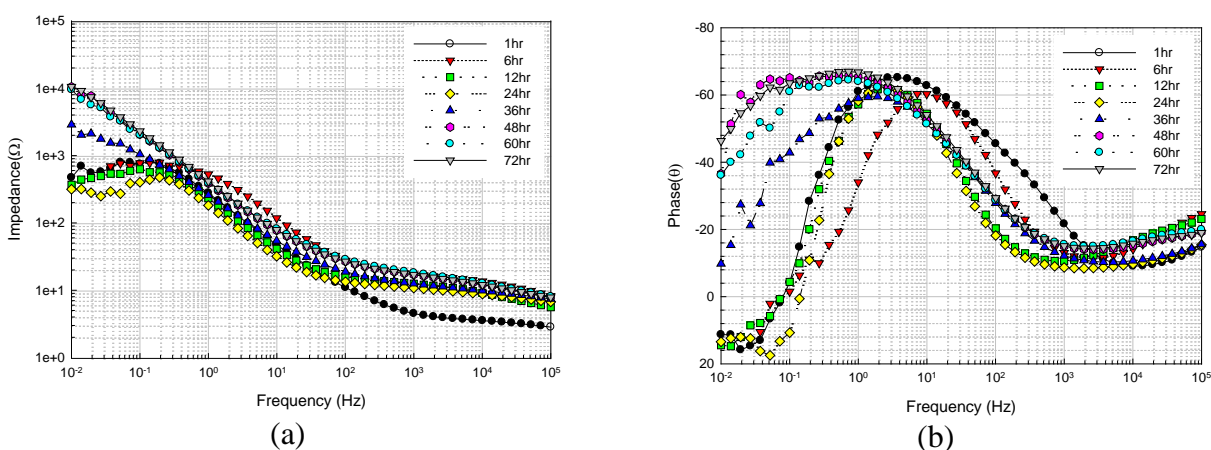


Figure 12. EIS plots of (a) impedance and (b) phase angle of carbon tow-CNT-AA2024 during 72-hr. immersion in 3.5 wt% NaCl.

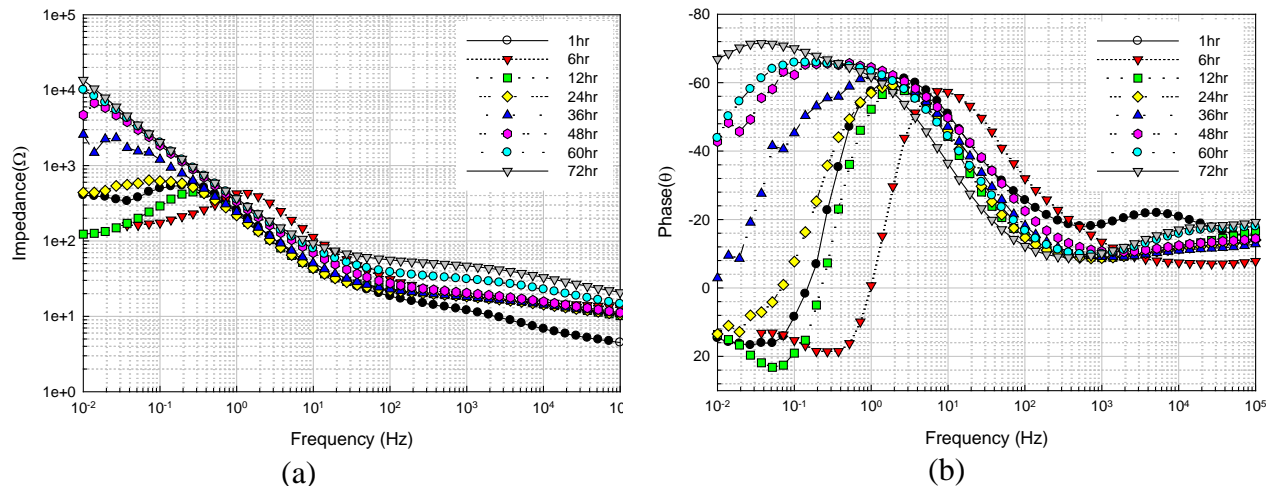


Figure 13. EIS plots of (a) impedance and (b) phase angle of carbon tow-CNT-AA7075 during 72-hr. immersion in 3.5 wt% NaCl.

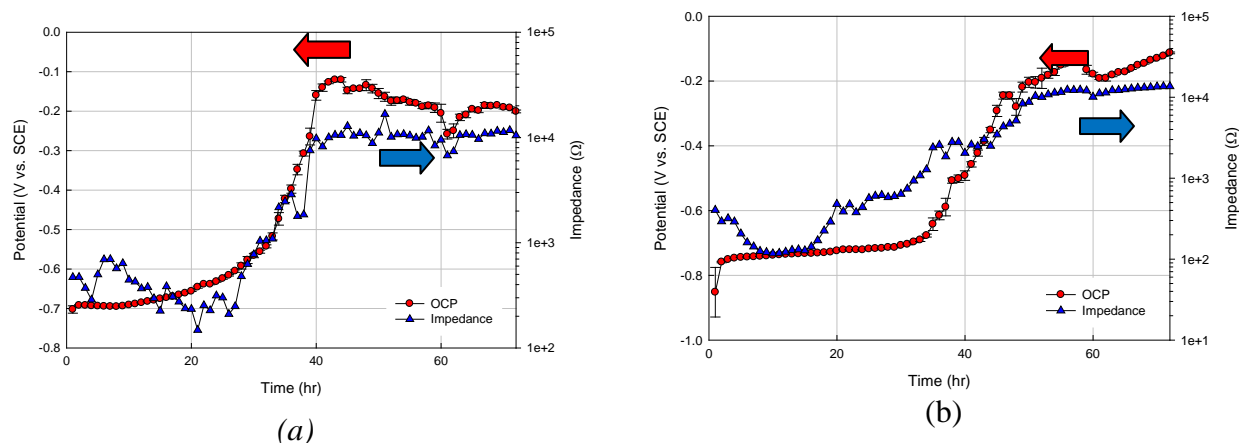


Figure 14. OCP and impedance plots of (a) carbon tow-CNT-AA2024 and (b) carbon tow-CNT-AA7075 during 72-hr. immersion in 3.5 wt% NaCl.

Figures 15 and 16 show the effect of CNT on the sensitivity of the carbon tow with AA2024 and AA7075 in 3.5 wt% NaCl. As can be seen, the impedance values of the carbon-CNT with AA2024 slightly decreased with increasing immersion time. The impedance values of the carbon-CNT with AA7075 at the high-frequency region were almost the same, while those values at the low-frequency region slightly increased. Figure 17 summarizes the changes of the OCP and impedance values for the carbon tows with AA2024 and AA7075 with increasing immersion time up to 48 hours immersion in 3.5 wt% NaCl solution. The variations of the OCPs have exactly the same trends as the carbon tow with aluminum alloy coatings in Figure 14. The change of the impedance values, however, is significantly different compared to the carbon tow with aluminum alloy coatings. This comparison suggests that the aluminum alloy coatings on the carbon tow-CNT dissolve and the impedance values, with increasing immersion time, tend towards the impedance of the carbon tow-CNT, similar to the carbon tow-CNT test values in Figure 4. It is also noted that the transition times of the carbon-CNT with AA2024 and AA7075 were around 10 and 20 hours, respectively, which indicates that CNT enhanced the dissolution of the aluminum alloy coatings on the carbon tows.

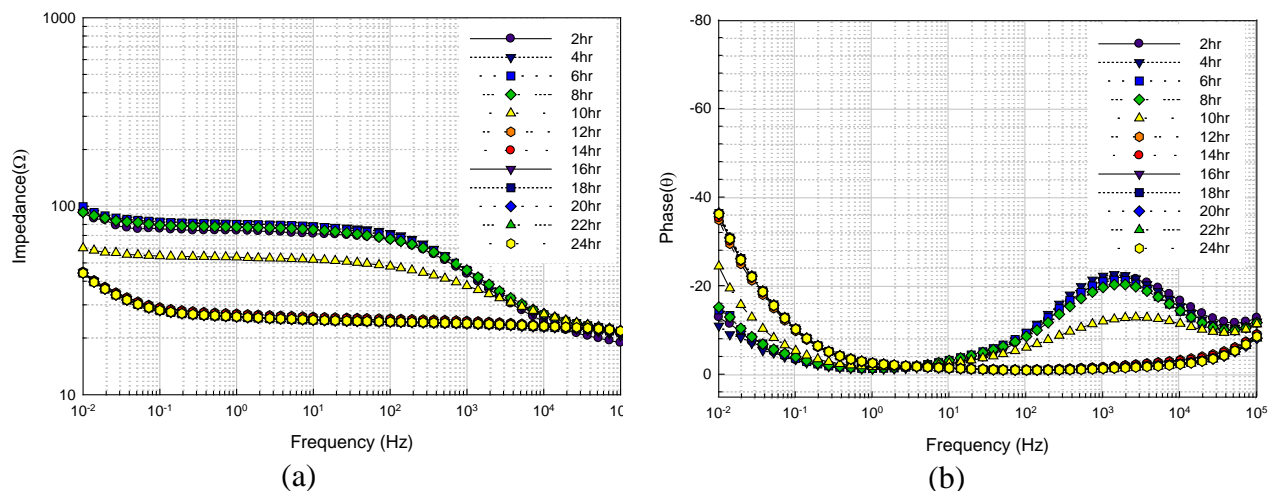


Figure 15. EIS plots of (a) impedance and (b) phase angle of carbon tow-CNT-AA2024 during 24-hr. immersion in 3.5 wt% NaCl.

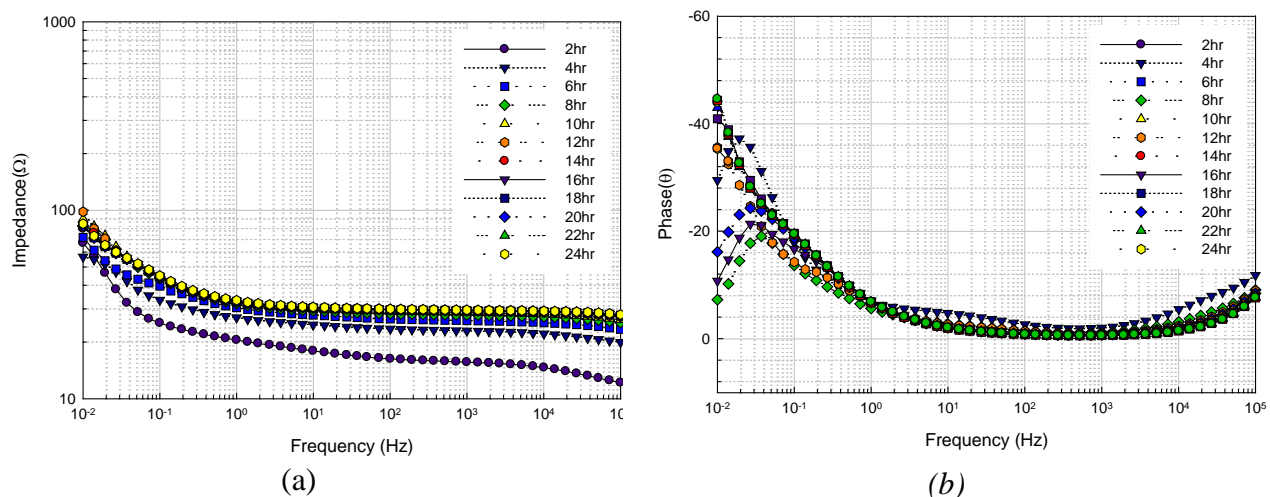


Figure 16. EIS plots of (a) impedance and (b) phase angle of carbon tow-CNT-AA7075 during 24-hr. immersion in 3.5 wt% NaCl.

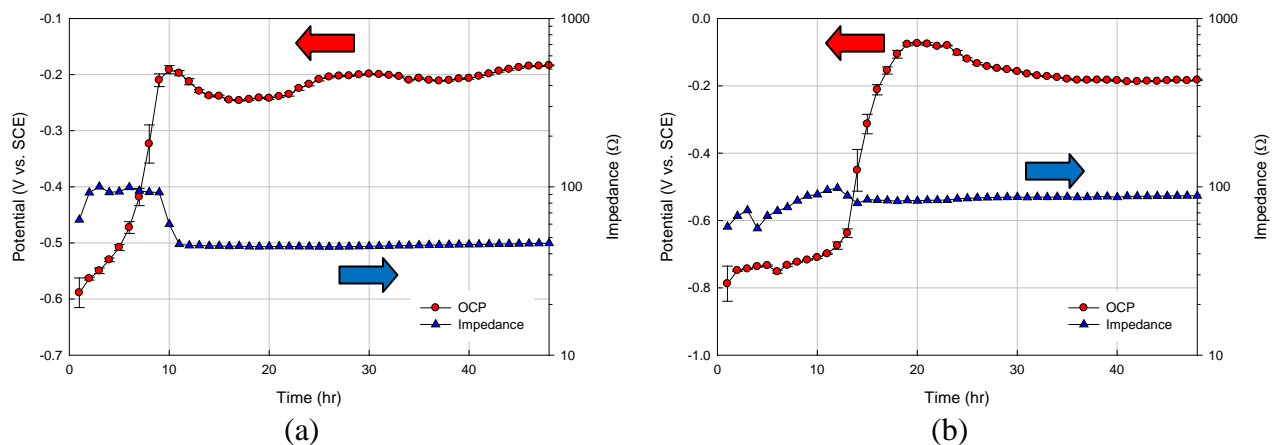


Figure 17. OCP and impedance plots of (a) carbon tow-CNT-AA2024 and (b) carbon tow-CNT-AA7075 during 48-hr. immersion in 3.5 wt% NaCl.

2.4 Summary and Recommendations

OCP/EIS measurements of CNT on the carbon tows suggest that the carbon tow with CNT exhibit higher potential and more conductivity than the carbon tow alone. SEM images and EDS measurements on the aluminum alloy coatings deposited on the carbon tows show the same chemical composition as the aluminum alloy substrates from the sputtering target. Measurements of the OCPs of the aluminum coatings also show the OCP values of the bulk aluminum alloys. The carbon-CNT with aluminum alloy coatings was more sensitive in monitoring the change of corrosion potential compared to the carbon tow with aluminum alloy coatings. In particular, transitions of OCP and impedance values of the carbon-CNT with aluminum alloy coatings occur about 10-20 hours after immersion in 3.5 wt% NaCl, while the transition of the carbon tow with aluminum alloy coatings took about 40 hours.

For the further investigation of the corrosion sensing behavior, individual sensor output during corrosion should be monitored and tracked against corresponding weight loss and chemical change as a function of time. In addition, the current project is conducted in NaCl solution. More realistically, the sensing behavior should be checked in the salt fog condition (ASTM B117) [28] and wet/dry cycling (GM 9540) [29], again, comparing sensor output to corresponding weight loss and chemical changes as a function of time. Under these same conditions, sensors also should be attached to structural aluminum coupons to monitor corrosion, correlating sensor output with coupon weight loss and surface condition.

Section 3

Mechanical Sensing

3.1 Objectives

The purpose of the mechanical sensing research was to investigate the use of fuzzy fibers as strain sensors. For this study, sensors were developed and then evaluated in several forms of specimens. The work included characterizing the strain sensor at fiber, tow, and coupon scales, then incorporating the sensor into representative composite specimen geometries and characterizing their behavior. A significant part of this effort was the development of data acquisition techniques to enable instrumentation to acquire and process sensor signals.

3.2 Technical Approach

To assess the strain-sensing capabilities of fuzzy fiber sensors, the experimental program first developed a suitable strain sensor, as well as the instrumentation to acquire and process sensor signals. The program then characterized the strain sensor as fibers, tows, monocomposites (embedded in epoxy matrix material), and as composite specimens. Coupon geometries were developed according to ASTM standards and designed to evaluate specific characteristics of the sensors of interest. Following successful evaluation of individual tows, single tows were then imbedded in an epoxy matrix monocomposite. At this stage, the fuzzy fiber strain sensors were considered mature enough to incorporate into carbon composite specimens designed to produce specific geometry-induced responses. These included straight-sided, stress-concentration, and Poisson's-effect specimens. All composite specimens were fabricated as both unidirectional $[0\pm]_8$ and orthotropic $[\pm 45^\circ]_{4s}$ fiber orientations.

The specific steps of technical approach may be summarized as follows:

- a) Sensor development
- b) Instrumentation development
- c) Fiber and tow tension tests
- d) Monocomposite tension tests
- e) Composite tests
 - Uniaxial and orthotropic coupon tension tests
 - Stress-riser tension tests
 - Poisson and off-axis tension tests.

3.2.1 Sensor Development

The fuzzy fiber sensor is created by the application of CNT in a continuous process which is applied to multifiber tows, in this case, composed of glass fibers. Attempts to separate single fibers from the coated tows resulted in a small bundle of four coated fibers which was used for an initial test of resistance as a function of strain. Next, complete (coated) tows were tested, but results were inconsistent. Finally, single tows were encased in epoxy to constrain them in a fashion more-closely approximating inclusion in a composite panel. Strain sensors developed later in the program for the composite panels took advantage of the knowledge gained in the fiber, tow, and monocomposite tests. Those experiments indicated that high-doping CNT produced the best strain response, so sensors were developed accordingly for use in the composite specimens. The initial batch of high-doping sensors had resistances on the order of 50 k Ω , while the second batch had resistances on the order of 3 k Ω . Low-doping sensors (with a resistance above 1 M Ω) were determined to be less-desirable and were not used in the test program beyond two initial tests. The process of em-

bedding sensors in a carbon composite panel required electrical isolation for the sensor. This isolation was provided by enclosing the sensor between two layers of E-2 e-glass having a 0/90 weave. The e-glass was 0.008" thick per layer, resulting in a 0.016" total veil thickness, with a typical veil width of 0.4". Veil length varied with the length of the fuzzy-fiber sensor. Instrumentation leads were, again, bonded to the fiber tow with conductive epoxy and extended beyond the veil. Representative sensors enclosed in the e-glass veil ready to be imbedded in composite laminate are shown in Figure 18.

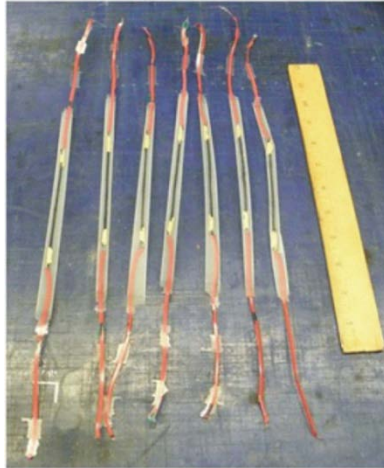


Figure 18. *Fuzzy-fiber sensors enclosed in electrical isolation e-glass veil.*

3.2.2 Instrumentation Development

Two types of signals indicating mechanical strain or damage are available from embedded fuzzy fibers. The first is a loss of continuity, indicating the complete breakage of the fuzzy fiber tow due to an overload or crack propagation. This mode was demonstrated in the initial fiber tow tests, but not pursued, due to its trivial nature. The second signal type is an increase in electrical resistance due to applied strain.

Initial electrical connections to fuzzy fiber tows used a mechanical clamp. While this worked on the carbon fiber tows used in an initial demonstration, it was ineffective on fuzzy glass fiber tows. Essentially, the fibers were disrupted by the connection, leading to the shedding of some nanotubes and inconsistent connectivity. The next method, used throughout the test program, was to use a silver-filled electrically conductive epoxy, Circuitworks CW2400, to bond the fuzzy fiber tow to a copper leadwire. This provided a reliable joint and a signal path out of the composite coupon. Magnet wire in the 30-36 AWG diameter range was used for lead wires from the sensors, between composite plies, to external instrumentation. Thinner wires were used for the initial tow tests where minimum force on the joint was required. An early example of the signal lead wire bonding is shown in Figure 19. A radiograph is shown in Figure 20 depicting the refinement typical of later examples.

The simplest way to monitor a resistance is to use a voltage divider. The voltage across the sensor can be measured and correlated with sensor resistance by placing a fixed resistor (of similar value to the sensor) in series with it and applying a fixed voltage across the two resistors. This worked for some bare tow and monocomposite tests, but was not sufficiently sensitive to use in composites. Instead, the sensor was incorporated into a typical Wheatstone bridge circuit and a Vishay 2310 signal conditioner was used to amplify the sensor response. A half-bridge circuit

was used, where one leg of the bridge is internal to the amplifier and the second leg consists of the sensor and a dummy resistor matching the sensor resistance. A resistance substitution box was used in the majority of the tests to simplify matching the value of the sensor and balancing the circuit. In early tests, data was collected with a National Instruments DAQPad 6020E; once automated testing began, this was switched over to a Scientific Solutions Labmaster DMA board in the controlling PC.



Figure 19. Initial conductive epoxy bond between fiber tow and instrumentation lead.



Figure 20. Radiograph of refined conductive epoxy bond between wire tow on left and instrumentation lead on right.

3.2.3 Fiber and Tow Tension Tests

Initial studies evaluated the sensor as a fiber tow. The carbon tows were evaluated to define testing requirements such as specimen gripping, independent strain measurement, and instrumentation. Fiber tows were tested in an MTS Bionix electromechanical test frame having a maximum load capacity of 2000 N. Fibers and tows were gripped by gluing them on card stock across a hole shown in (Figure 21). The card stock was then gripped in the load frame, then carefully severed on both sides of the hole, such that the fiber or tow was carrying all the applied load. Initial specimens were unusable due to the glue (cyanoacrylate) wicking into the fiber tow and blocking the conductivity path. A secondary mounting method was developed that used a silver-filled conductive epoxy (Circuitworks CW2400 or equivalent) to bond the tow to the cardstock, with a 36AWG magnet wire also embedded in the epoxy to serve as a leadwire. After a small manual preload, the bridge was balanced and the test continued in stroke control, at a rate of 0.0001 inch/minute. The fiber was connected as one arm of a Wheatstone bridge and a Vishay 2310 amplifier was used to amplify the signal, which was recorded simultaneously with load and stroke. Low-doping bundles had resistances in the 5 M Ω range; high-doping bundles were in the 10 to 20 k Ω range. Prior to the tow tests, a bundle of four fibers was separated from a tow and tested with a load range of 200 grams.

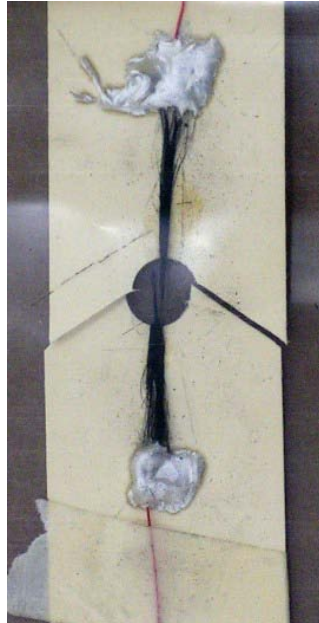


Figure 21. *Post-test fuzzy fiber tow.*

3.2.4 Monocomposite Tension Tests

Single-tow monocomposite specimens were fabricated using both low- and high-resistivity (from thicker and thinner coatings of CNT) fibers. Specimens were cast in a mold made of RTV664B moldmaking compound from Momentive Performance Materials. The monocomposite specimen epoxy, made up of Epon E-682 Epoxy Resin and Hexion cure agent W (Epikure), was mixed at a ratio of 100:32 by weight. Initial fiber tow resistance was ~180 kOhm and, following epoxy infiltration, increased to ~360 kOhm. The monocomposite specimen was cured at 250° F for 2 hours and then 350° F for 2 hours. A representative specimen is shown in Figure 22. Specimens were tested in a hydraulic test system as shown in Figure 23.

The test system consisted of an MTS 458 analog controller and 100kN servoactuator; instrumentation included a load cell (S/N 5772) with a 10 kN range and a knife-edge MTS extensometer (S/N1125). Tests were run in load control, at a ramp rate of 10 N/s. Data was, again, simultaneously recorded with load, strain, stroke, and sensor output recorded. A hydraulic clamping grip was used with no tabs. Initial tests were run with a simple voltage divider and no amplification used for the sensor signal; a Wheatstone bridge, with various gain settings, was again used to amplify the sensor signal in the later tests. Refinements made in the monocomposite fabrication process included minimizing the formation of bubbles within the epoxy, optimizing the mold used to cast the specimen, trying different epoxies, and improving the instrumentation connections to the fiber tow.



Figure 22. *Epoxy matrix monocomposite with imbedded fiber tow.*

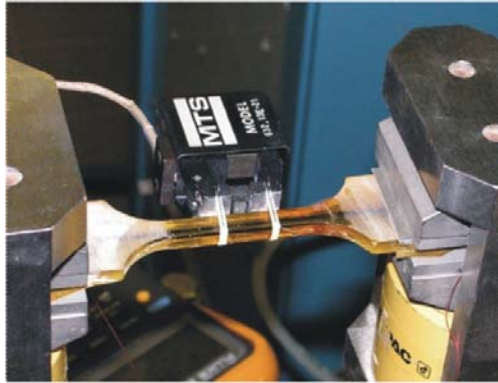


Figure 23. *Testing of monocomposite in a hydraulic test system with an extensometer to measure strain.*

3.2.5 Composite Tests

All composite specimens were fabricated through a similar process. Six composite panels, 12 " × 12", were fabricated with IM/977-2 material. Three panels each were prepared with unidirectional $[0]_8$ or orthotropic $[\pm 45]_{4s}$ layups. Sensors were embedded at specified levels in the layup, as shown in Figure 24, depending on the type of specimen response to be tested. Panels were then processed in an autoclave per the IM7/977-2 recipe for standard prepreg autoclave cure and bagging procedure. This required a 540-minute total process with 360 minutes at 355° F part temperature and 100 psi pressure. Panels prepared for the autoclave are shown in Figure 25. Following cure, specimens were machined from the panels using an abrasive saw as shown in Figure 26.



Figure 24. *Composite panel layup with embedded sensors.*

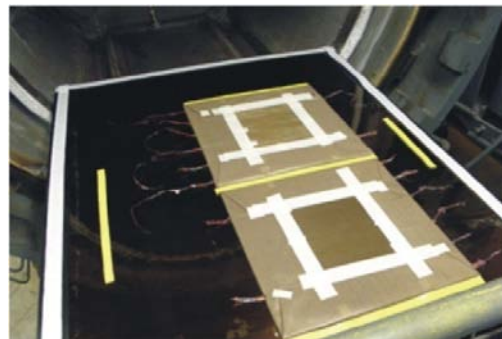


Figure 25. *Panels in preparation stage for autoclave cure.*



Figure 26. *Use of an abrasive saw to machine specimens from panels.*

3.2.5.1 *Uniaxial and Orthotropic Coupon Tension Tests*

Two composite panels, one for each layup ($[0]_8$ or $[\pm 45]_{4s}$), were fabricated with 6' -long fuzzy fiber strain sensors embedded at the midpoint of the laminate plies. A completed panel is shown in Figure 27. Eight straight-sided specimens (as shown in Figures 28 and 29), were machined from each panel and tested in a hydraulic test system.

The test system consisted of an MTS 458 analog controller and 100kN servoactuator in a vertical load frame, as shown in Figure 30; instrumentation included a load cell (S/N 1858) with a 20 kN range and a knife-edge MTS extensometer (S/N1962) with a 25mm gage length. Tests were run in stress control at ramp rates of 0.2, 2.0, and 20 MPa/s. Data was, again, simultaneously recorded with load, strain, stroke, and sensor output recorded. A large hydraulic wedge clamping grip was used with tabs on the specimens. A Wheatstone bridge and Vishay 2310 amplifier with a gain setting of 100 was, again, used to amplify the sensor signal. Uniaxial tests were stopped at 400 MPa and Orthotropic tests were stopped at 40 MPa stress. After inserting the specimen in the load frame and stabilizing the load near zero, these specimens were surrounded by a fiberglass blanket to isolate them from ambient air and allowed to thermally stabilize before testing. Tests at slower rates were repeated if substantial offsets in sensor signal were noted after a test, indicating thermal drift. Sensors in these tests had a nominal resistance in the 50 k Ω range.

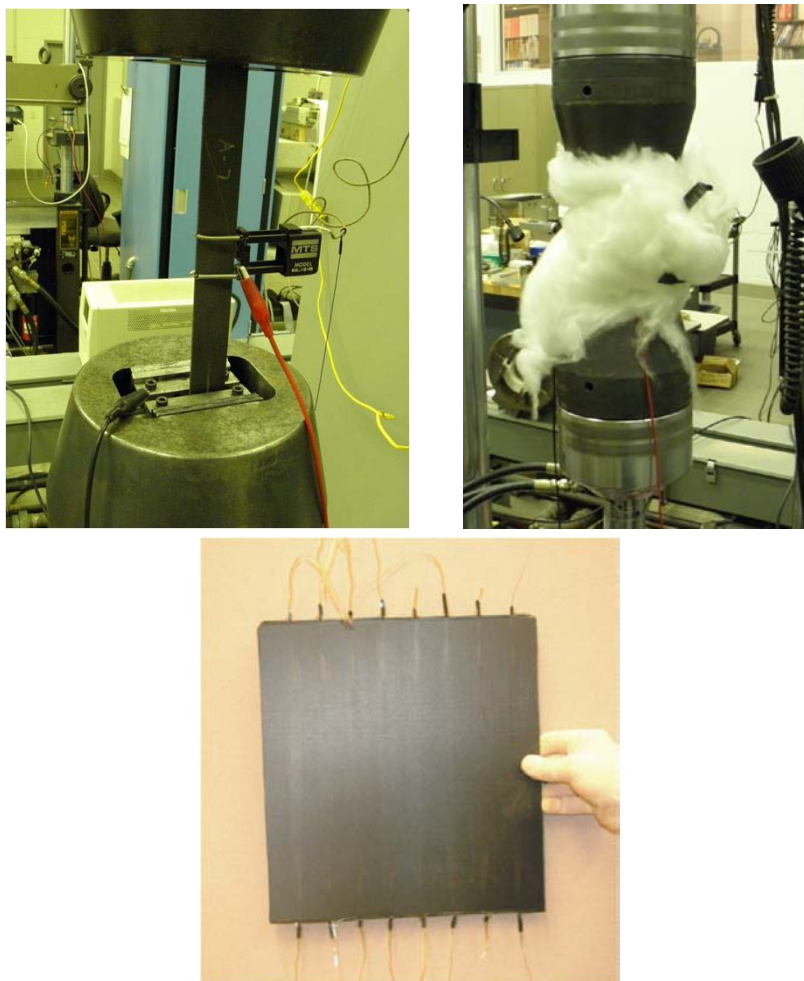


Figure 27. Composite panel with embedded strain sensors oriented for straight-sided specimens.



Figure 28. Straight-sided specimen for strain sensitivity measurements.

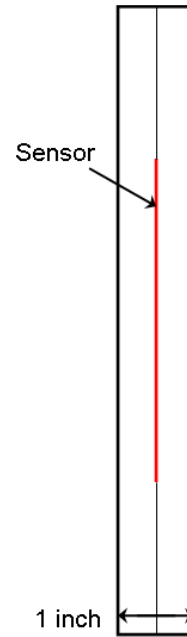


Figure 29. Schematic of straight-sided specimen with imbedded sensor depicted in red.



Figure 30. Test system consisting of an MTS 458 analog controller and 100kN servoactuator in a vertical load frame.

Sixteen specimens in total were tested and initial specimen parameters are shown in Table 1.

Table 1. Straight-Sided Specimen Parameters

Specimen ID	Measured Resistance (kilo ohm)	Width 1 (mm)	Width 2 (mm)	Thickness – End (mm)	Thickness – Middle (mm)
[0] ₈					
0-1	50.9	25.49	25.18	1.32	1.21
0-2	32.8	25.11	25.38	1.32	1.14
0-3	50.4	25.21	25.46	1.29	1.17
0-4	49.2	25.45	25.23	1.31	1.18
0-5	51.5	25.45	25.22	1.37	1.21
0-6	76.3	25.17	25.31	1.25	1.14
0-7	59.2	25.42	25.27	1.29	1.18
0-8	57	25.46	25.15	1.33	1.18
[+/-45] _{4s}					
A-1	50.9	25.37	24.83	2.3	2.15
A-2	48.9	25.31	24.73	2.35	2.19
A-3	56.3	25.18	24.71	2.31	2.19
A-4	44.5	24.55	24.93	2.32	2.16
A-5	51.3	25.75	25.55	2.33	2.17
A-6	48.4	25.63	25.64	2.32	2.17
A-7	51.3	25.48	26.46	2.26	2.11
A-8	102.4	24.68	25.36	2.35	2.18

3.2.5.2 *Stress-Riser Tension Tests*

Two specimens were designed to further study the fuzzy-fiber sensor behavior in response to stress. An “open-hole specimen” was developed based on ASTM Standard D 5766 “Standard Test Method for Open-Hole Tensile Strength of Polymer Matrix Composite Laminates.” The specimen contained two 3.0”-long sensors to evaluate the response to near- and far-field stresses around an open hole. In accordance with D 5766 [30], the “width-to-diameter ratio” was maintained through the use of a 3”-wide specimen and a 1/2”-diameter hole. Two composite layups were fabricated: unidirectional ([0]₈) and orthotropic ([± 45]_{4s}).

Eight fuzzy-fiber sensors were embedded in each layup, two for each specimen, in the longitudinal direction (parallel to the 0 degree unidirectional fibers), as shown in Figure 31. Sensor position was determined by the eventual location of a hole to be machined at the longitudinal midpoint and mid-width of the specimen.

Sensors were located at the midpoint of the panels as shown below for the unidirectional and orthotropic layups:

$$[0^\circ / 0^\circ / 0^\circ / 0^\circ / \text{Sensors} / 0^\circ / 0^\circ / 0^\circ / 0^\circ]$$

$$[+45/-45/+45/-45/+45/-45/+45/-45 / \text{Sensors} / -45/+45/-45/+45/-45/+45/-45/+45]$$

Laminates were processed in an autoclave and final form is shown in Figure 32.

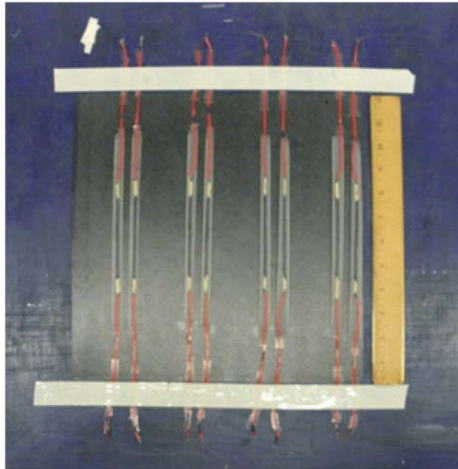


Figure 31. Sensors positioned during composite panel fabrication.

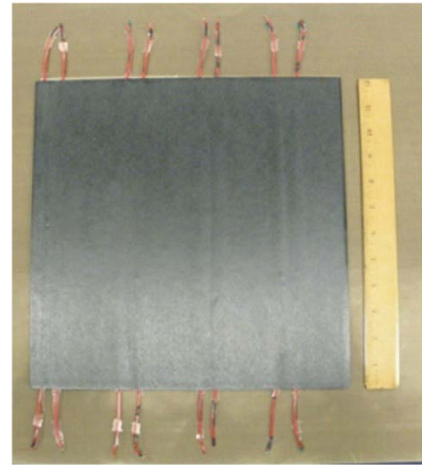


Figure 32. Fabricated panel with embedded sensors.

Four specimens were then removed from each panel, cutting parallel to the sensors. A representative specimen is shown in Figure 33 and specimen schematic in Figure 34. Following initial mechanical tests, open holes were machined in the specimens to create the stress concentration. Stress-concentration specimen parameters, as measured prior to testing, are shown in Table 2. Test setup was essentially the same as for the earlier tension tests, described in Section 2.2.5.1, except for the addition of a second channel of sensor amplifier and data collection. In addition, the extensometer was moved away from the hole in later tests in order to reduce the influence of the stress concentration on the reference strain data. Finally, sensors were 3000 Ω nominal, rather than 50 k Ω , and the uniaxial stress was limited to 200 MPa



Figure 33. Open-hole stress-concentration specimen prepared for testing.

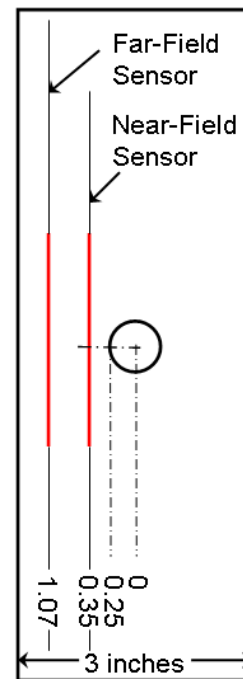


Figure 34. Schematic representative of the sensor locations.

Table 2. Open-Hole Stress-Concentration Specimen Parameters

Specimen ID	Measured Resistance (kilo ohm)	Width (mm)	Thickness (mm)
	Near-Field/Far-Field		
HU-01	3.05 / 3.20	73.3298	1.2446
HU-02	3.74 / 3.38	74.7649	1.2319
HU-03	2.45 / 2.47	75.7809	1.0922
HU-04	3.20 / 2.63	74.3839	1.0668
HQ-01	2.43 / 2.42	74.8538	2.2479
HQ-02	2.42 / 2.50	76.7334	2.2606
HQ-03	2.47 / 2.49	74.9808	2.159
HQ-04	2.79 / 4.55	76.9493	2.1336

3.2.5.3 *Poisson and Off-Axis Tension Tests*

Specimens were designed and fabricated to evaluate sensor response in both longitudinal and transverse orientations relative to the loading axis. The specimens were fabricated in both $[0^\circ]_8$ and orthotropic $[\pm 45]_{4s}$ layups. Two 3.0" long fuzzy fiber sensors were embedded in each layup, one in the longitudinal direction (parallel to the 0° unidirectional fibers) and the second in the transverse direction (perpendicular to the 0° unidirectional fibers) as shown in Figures 35 and 36. Removal of the specimens from the panel by machining a cut parallel to the longitudinal axis necessitated that all sensor instrumentation wires exit the specimen along its ends rather than sides. The sensors were placed between plies (as shown below) for each layup where TS = transverse sensor and LS = longitudinal sensor:

$$[0^\circ / 0^\circ / 0^\circ / \text{TS} / 0^\circ / 0^\circ / \text{LS} / 0^\circ / 0^\circ / 0^\circ]$$

$$[+45/-45/+45/-45/+45/-45/ \text{TS} /+45/-45/-45/+45/ \text{LS} /-45/+45/-45/+45/-45/+45]$$

Laminates were processed in an autoclave and then machined to a shape that would optimize the transverse sensors response to Poisson effects. Final specimen configuration is shown in Figure 37.

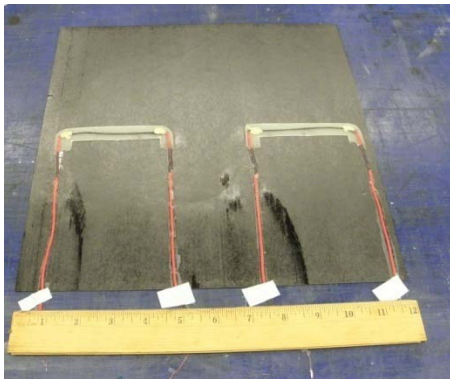


Figure 35. Insertion of fuzzy fiber sensors in the transverse orientation.

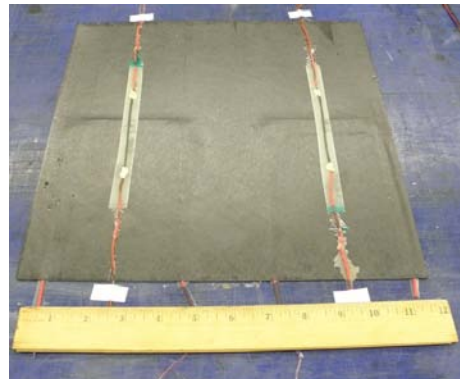


Figure 36. Insertion of fuzzy fiber sensors in the longitudinal orientation.

Figures 37 and 38 show the specimen in final form and a schematic with sensor locations.



Figure 37. Final form of Poisson's specimen.

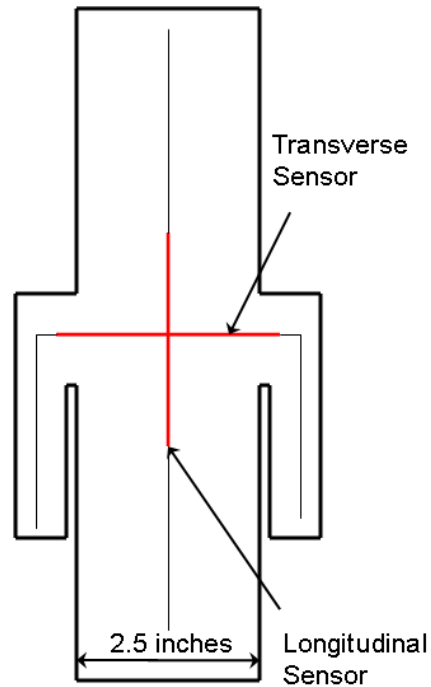


Figure 38. Schematic with sensor locations.

Initial specimen parameters are shown in Table 3 and a specimen gripped in a hydraulic test system is shown in Figure 39. Test setup was essentially the same as for the earlier tension tests, described in Section 2.2.5.1, except for the addition of a second (transverse) channel of sensor amplifier and data collection. Again, the extensometer was moved from the center of the specimen to a section of uniform area. In a second set of tests, the specimens were modified to lengthen the kerf connecting the “body” to the “arms” of the specimen. Sensors in these tests had a nominal resistance in the 50 k Ω range and the uniaxial maximum stress was limited to 200 MPa.

Table 3. Poisson Ratio Specimen Parameters

Specimen ID	Measured Resistance (kilo ohm)	Width 1 (mm)	Thickness – Center (mm)	Thickness – Edge (mm)
	Longitudinal/Transverse			
AT-1	23.95 / 48	68.7	2.34	2.15
AT-2	19.93 / 45	67	2.38	2.18
OT-1	9.75 / 17.38	63.2	1.55	1.33
OT-2	13.85 / 41.6	61.8	1.47	1.28



Figure 39. *Final specimen configuration with longitudinal and transverse sensors installed in the materials test system.*

To further investigate sensor response to longitudinal, transverse, and off-axis loading conditions, a unique specimen was fabricated from [0/90] weave 8821 fiberglass (e-2 eglass) and epoxy. The 11-ply specimen contained 4 independent sensors at individual layers in the laminate. The fabricated and machined specimen is shown in Figure 40.

This specimen was tested in another MTS servohydraulic test system with smaller hydraulic wedge grips open on the sides and a digital controller. No reference extensometer was used, but three channels of sensor data were collected at a time. The nominal resistance of these sensors was lower than those used in previous tests, now in the 3000Ω range. Tests were run dynamically, with a triangle wave of 0 to 1000 lb applied at 0.3 and 0.03 Hz. This load was applied to opposite arms of the specimen, while sensor response was monitored in three of the four possible directions. In order to cancel any effects from sensor location or fabrication, the test sequence was structured so that three channels were connected and, then, the response was recorded to load applied across each of the four sets of arms. One amplifier was moved to the previously unmonitored channel and the test sequence was repeated.

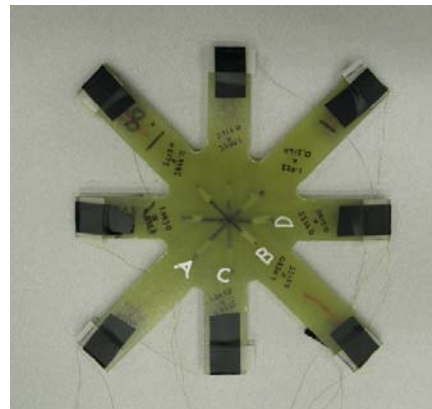


Figure 40. *Sensor-orientation specimen.*

3.3 Results and Discussion

The series of tests noted above progressed from an initial sensor feasibility study to incorporation in segments of actual composite panels. The sensors were shown to produce consistent response, low noise, high strain capability, and repeatable for elastic strain in same specimen (no hysteresis or offset)

3.3.1 Fiber and Tow Tension Tests

It proved impractical to separate individual fibers from a tow for testing. A bundle of four fibers was successfully separated from a tow and tension tested to failure. Figure 41 shows the data from this test. As the load increased, there was an upward trend in the strain response, up until the first instance of fiber breakage occurred, which sent the amplifier out of range. Note the four individual load-shedding events marking the failure of the four fibers in the bundle. This test was treated as a rough proof-of-concept and testing progressed to complete fiber tows. No more single- (or several-) fiber tests were pursued because of doubts if they would exhibit representative behavior that would relate to that of a fuzzy fiber tow in a composite panel.

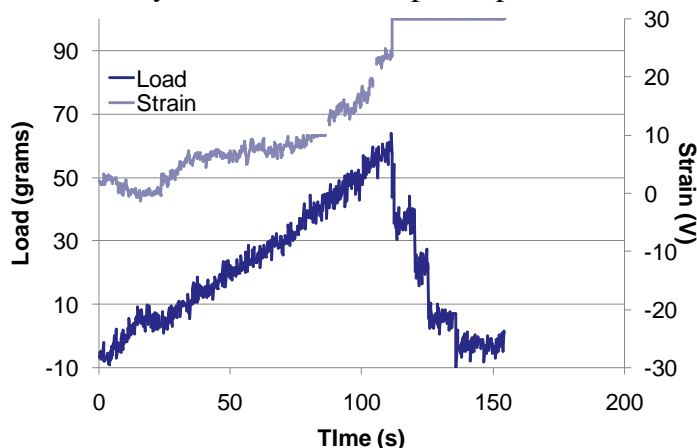


Figure 41. Four-fiber data.

A number of tests of fiber tows were conducted, with tows of both low and high doping. Figure 42 shows the results of a low doping test, with a nominal resistance of 5 Ω . While a trend of resistance increase with load (and strain) can be seen, it is quite noisy. A second test had similar results. The high-doping specimens, with a typical response shown in Figure 43, had much-lower noise and lower resistance (10-20 k Ω). The initial response is especially promising, but the plateaus following the initial response were worrisome, especially after this trend was repeated in four specimens, but with wildly different values. It was determined that a likely cause was the unconstrained fibers that make up the tow were shifting as load was applied, essentially modifying the sensor. As a result, further tow tests were suspended, in favor of constraining the fibers within a matrix material to better simulate service conditions.

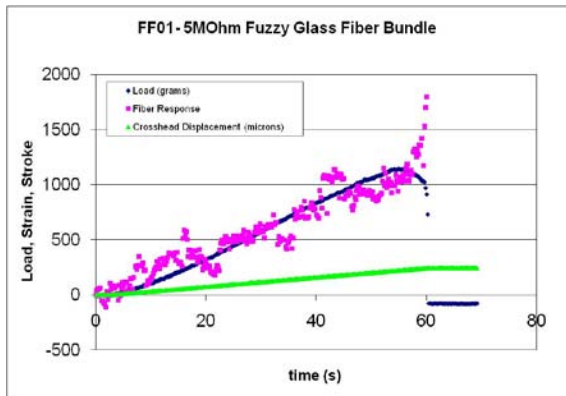


Figure 42. Low-CNT doping initial data.

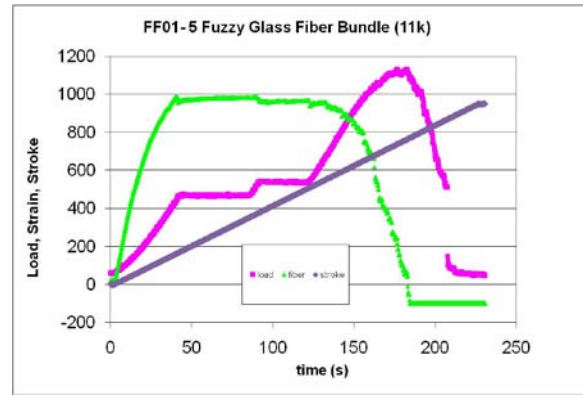


Figure 43. High-CNT doping initial data.

3.3.2 Monocomposite Tension Tests

Monocomposite refers to a single tow of fuzzy fibers encased in an epoxy matrix that comprises the majority of the specimen. Figures 44 and 45 show typical initial results from this testing. Both low- and high-doping tows were tested and, while both showed similar promise, the high doping was selected for further work because it was likely to have resistances closer to standard strain gage values, as well as lower noise and higher sensitivity. Figure 46 shows the results from the next generation of monocomposites; this figure actually shows four separate tests on the same specimen. The darkest symbols are the initial tests, with several short load ramps (darkest), then another ramp-up until damage is registered, and an unloading ramp. The slope variation in the initial loadings is of concern, but the fact that the slope is the same for both loading and unloading is encouraging for use as a sensor. Preliminary calculations of the gage factor for this sensor indicated a value of approximately ten, indicating ample sensitivity.

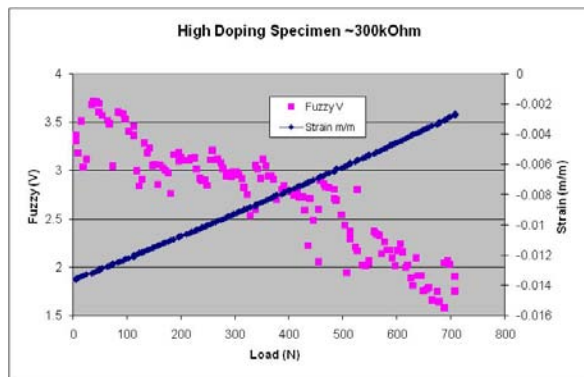


Figure 44. Initial low-doping monocomposite data.

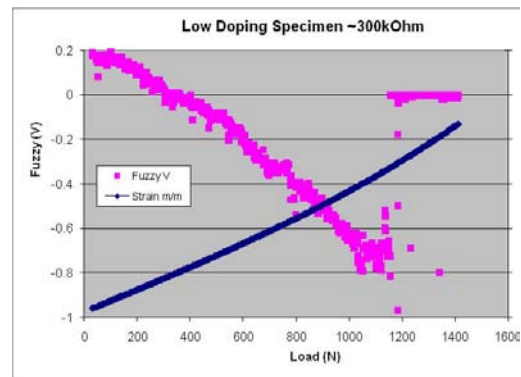


Figure 45. Initial high-doping monocomposite data.

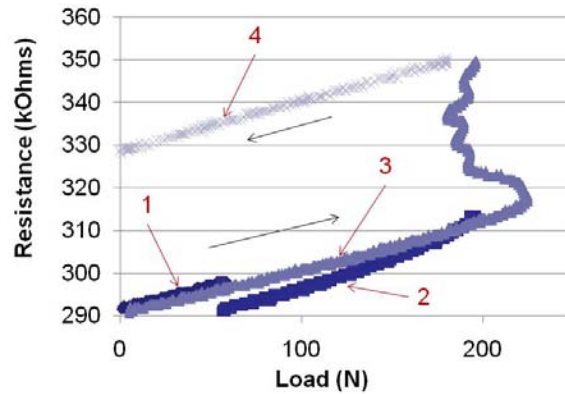


Figure 46. *Monocomposite intermediate test series.*

Due to inconsistencies in monocomposite fabrication, the process was changed as noted above and additional tests were run with the improved sample. Figure 47 shows the resulting curves when tested to failure, with an extensometer strain measurement reference. The improved specimens displayed low noise, a consistent response in the elastic region, and reasonable linearity and sensitivity. In addition, they showed the potential for measurement of high strains, well above 1 percent. This was very encouraging and provided enough confidence to move on to the next phase, incorporating the sensor into an actual composite panel.

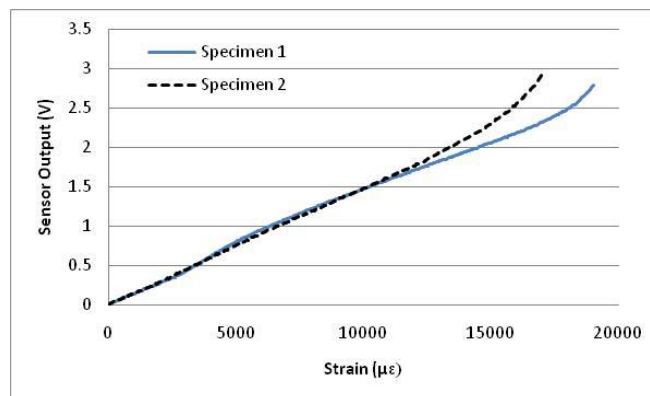


Figure 47. *Final format monocomposite strain data.*

3.3.3 Composite Tests

Based on the experience with tows and monocomposites, fuzzy fiber sensors were incorporated into composite panels, as noted above, and tested in tension, as well as tension near a stress riser. Additional tests were performed in order to investigate the response of the sensor to off-axis loading, including normal to the loading direction.

3.3.3.1 Uniaxial and Orthotropic Coupon Tension Tests

Once the test protocol was developed, tension tests showed that sensor response was insensitive to loading rate, but dependent on composite layup. Typical data is shown below in Figures 48 and 49. In both cases, the sensitivity (slope) is almost identical at all loading rates, with slight separation at higher strains. The mean response for 22 tests performed on seven uniaxial specimens was $0.58 \text{ mV}/\mu\epsilon$, with a standard deviation of $0.06 \text{ mV}/\mu\epsilon$. The mean response for 20 tests performed on six orthotropic specimens was lower ($0.41 \text{ mV}/\mu\epsilon$), again, with a standard deviation of $0.06 \text{ mV}/\mu\epsilon$. The actual data from these tests is shown in Figure 50. If not for the initial outlier, which is un-

explained, the orthotropic test standard deviation would have been even lower. Possibly, the additional scatter in the uniaxial data is caused by its higher stiffness or a complex state of stress around the sensor tow; thermal effects (described below) may also play a significant role and might explain the difference in scatter between the two layups. These responses give a mean gage factor for the uniaxial sensor of 2.3 and a gage factor of 1.6 for the orthotropic layup, similar to metal foil gages.

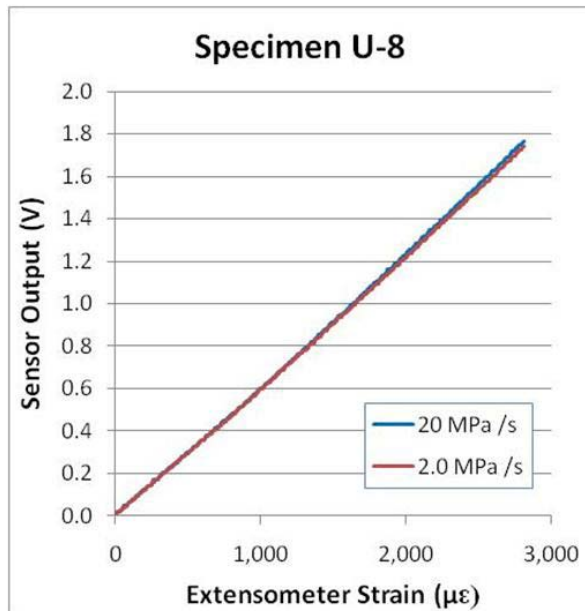


Figure 48. Uniaxial specimen strain data.

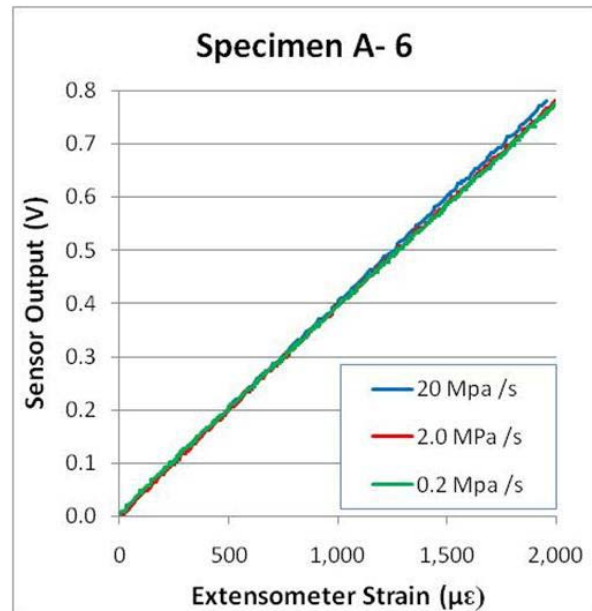


Figure 49. Orthotropic specimen strain data.

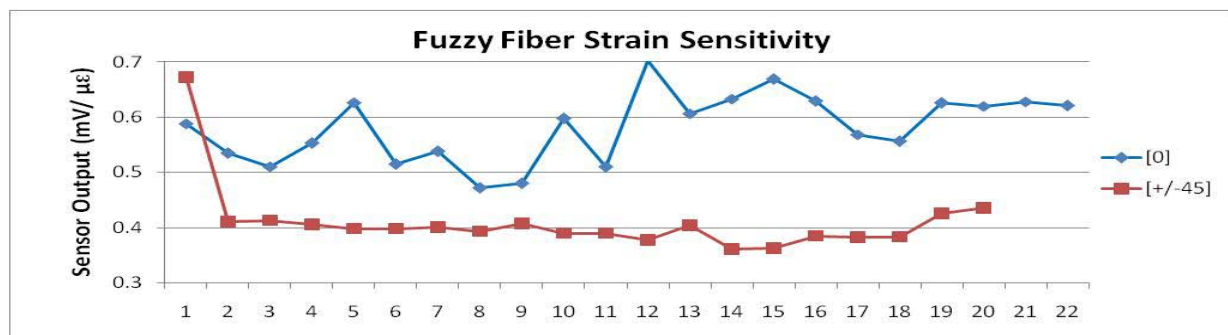


Figure 50. Tension test sensitivity.

3.3.3.2 *Stress-Riser Tension Tests*

The stress-riser tests consisted of tension tests before and after a hole was drilled near a sensor. The intent was that a sensor near the hole would have increased response to strain, due to the increased local stress, as compared to a far-field sensor at a distance from the hole. The first test before drilling the hole was used to establish baseline sensitivity for the sensors for comparison purposes. Figure 51 shows the stress riser specimen data. In this figure, S1 is the far-field sensor and S2 denotes the sensor close to the hole that was drilled. These sensors came from a second batch and had substantially lower resistance (3 k Ω as opposed to 50 k Ω); however, their overall sensitivity to strain was similar to the tension test data from the first batch.

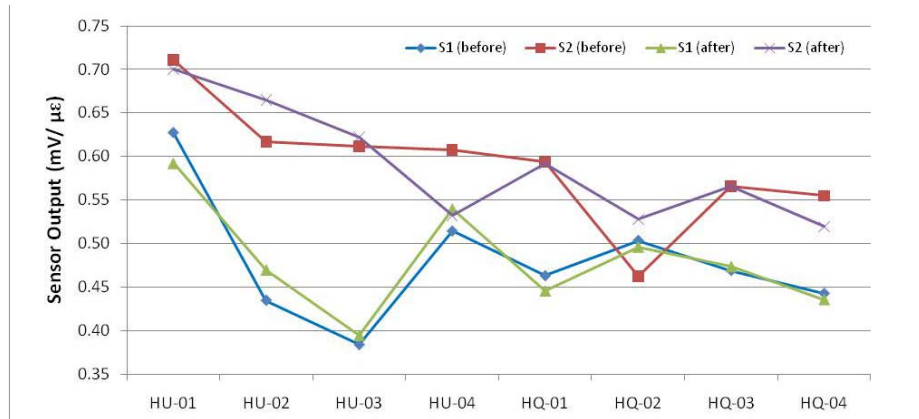


Figure 51. Stress-riser specimen data.

The first four sensors (HU-nn) are the uniaxial layup and the last four (HQ-nn) are the orthotropic layup. While the uniaxial sensors have a higher response than the orthotropic sensors, this effect is not as large as in the higher-resistance sensors. A more-pronounced effect is the consistently lower response from S1, the sensor located near the edge of the specimen. This may indicate a different state of stress than seen by the more-central sensor. Again, it appears that the orthotropic layup sensors exhibit lower scatter.

Of greater interest is the apparent response to the stress-riser – there does not appear to be a significant change in response due to the addition of the stress-riser. Further investigation revealed that this is due to the test construction rather than a sensor deviation from expected values. The near-field sensor has a 75 mm gage length and is located approximately 2.5 mm from the edge of the hole. Theory predicts a stress intensity factor of 1.3 (uniaxial) or 1.7 (orthotropic) at this location [31]. However, this factor is applied to a small portion of the overall sensing length, so is not readily apparent in the data. It would be possible to fabricate a short sensor to detect stress-risers (such as crack growth) in a specific location, but a long sensor is unlikely to show a defect until it grows through the sensing fiber, severing it.

3.3.3.3 *Poisson and Off-Axis Tension Tests*

To further investigate the different response of nominally identical sensors in different layups, additional tests were performed to look at the response of the sensors to off-axis or normal loading. The first of these used a wider specimen, with sensor fibers running both parallel and perpendicular to the loading direction. These sensors were from the first, higher-resistance batch and had a 3" gage length. The complex specimen design, required to accommodate the sensor lead wires during the autoclave process, likely caused some stress nonuniformity in the sensor area, as compared with the strain measured by the reference extensometer. Two uniaxial and two orthotropic specimens were fabricated and tested.

The response of the sensors aligned with the loading direction was, again, consistent with the initial tensile tests, with a uniaxial sensitivity of 0.67 mV/μ ϵ and an orthotropic sensitivity of 0.38 mV/μ ϵ . For the orthotropic layup, the transverse sensor showed a response of -0.13 mV/μ ϵ , an expected value for a Poisson's ratio of ~0.3. This is because, as the specimen elongated, it contracted laterally, and the sensor became shorter. The uniaxial specimens were not consistent with predictions. These should have had a much-higher Poisson's ratio and, therefore, stronger lateral contraction. However, the transverse sensors showed a positive response, 0.12 mV/μ ϵ , as shown in Figure 52. In order to confirm the observed behavior, the cut around the transverse

sensor leads was lengthened and the test was repeated. The goal was to check for a non-uniform response due to the extra material and, also, to guarantee that the experiment had been set up correctly. One specimen of each layup was retested in this fashion, with no substantial change in sensor response. An additional test along the third axis consisted of placing the flat specimen between compression platens and applying a compressive stress; the sensor had zero response to this loading. It is thought that there is a complex interaction between interlaminar stresses and the CNT conduction mechanism. For instance, the compressive load likely had no response because the autoclave cure likely densified their arrangement, such that additional compression did not cause an increase in conductivity. A related effect may have occurred in the transverse sensors.

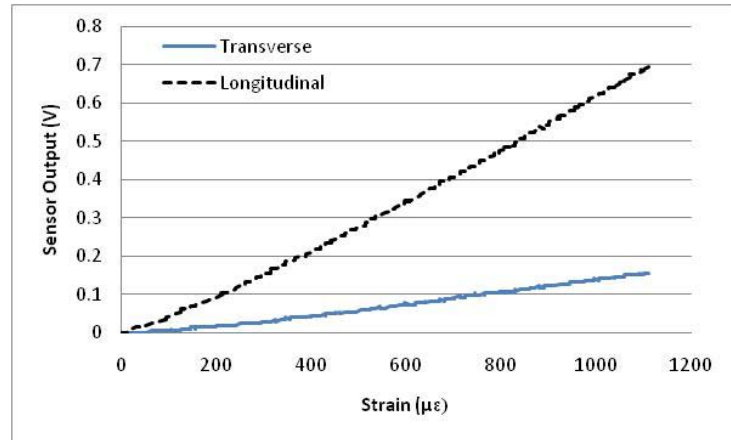


Figure 52. *Sensor response in uniaxial composite loaded along its axis.*

In order to further investigate these effects, the star-shaped fiberglass specimen described above was used to look at the longitudinal, transverse, and off-axis response for four sensors. In general, these performed similarly to the orthotropic sensors in the graphite-epoxy composites described above. Figure 53 shows the data from one test, where the specimen was loaded along axis “A”. The sensor aligned with the loading had the highest response, the sensor at 45° to the loading had a lower positive response, and the sensor at 90° to the loading showed a negative response because of Poisson effects. Due to the lack of a reference strain measurement, the magnitude of these sensitivities cannot be compared directly with results from previous sensors.

Figure 54 is a compilation of the sensitivity results from all tests on this specimen, with each data point representing the average of six, twelve, or 24 tests, depending on the sensor and the sensing mode. Data from all sensors was recorded with loading along all axes. In every case, the strongest response was in the longitudinal mode, followed by the oblique mode, and, finally, by the transverse mode, which was negative (or zero for sensor D). Some geometry effect is apparent, as sensors A and B were in the longer arms of the star and C and D were in the shorter arms. The gage length for all four sensors was the same. These tests confirmed the behavior of the fuzzy fiber sensors in an orthotropic composite, but did not provide insight into the anomalous transverse behavior in the uniaxial layup.

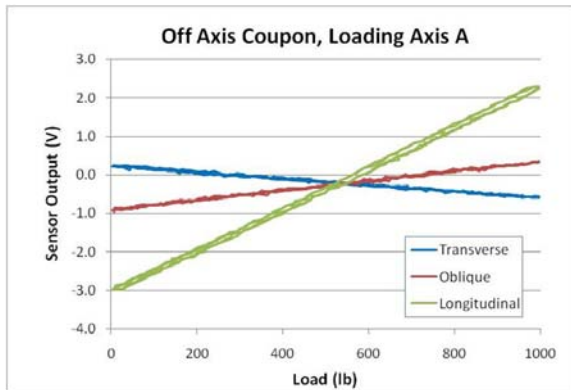


Figure 53. Typical off-axis sensor response.

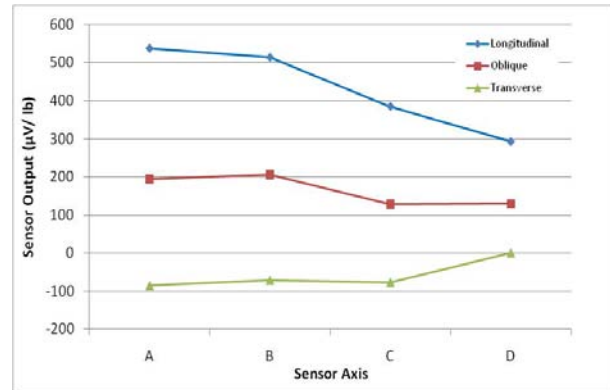


Figure 54. Off-axis sensitivity data.

3.3.3.4 Thermal Sensitivity

At the beginning of tensile testing, substantial thermal response was observed, causing unacceptable drift in the strain signal, as shown in Figures 55 and 56. Faster testing minimized this effect, but would have prevented the investigation of rate effects. Insulating the specimen from the air and allowing it to thermally stabilize before testing overcame the thermal issues. However, a separate investigation was performed to determine the magnitude of error in strain measurement that could be expected due to thermal errors. For this testing, the specimen was placed in a varied-temperature water bath and the resistance of the sensor was measured across a range of temperatures. The test was performed with one specimen incorporating a first batch ($\sim 50 \text{ k}\Omega$) sensor and one with a second batch ($\sim 3 \text{ k}\Omega$) sensor. Figure 57 shows the thermal response of the sensors. This is a substantial change in resistance, as it corresponds to a potential error on the order of $2000 \mu\epsilon/^\circ\text{C}$. Temperature compensation of deployed sensors is indicated if static strain or changes over time are required to be measured.

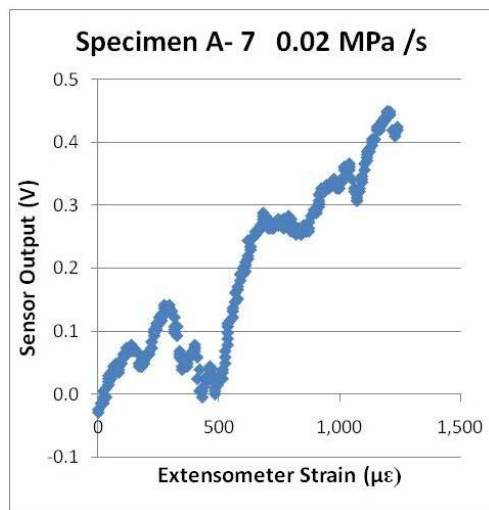


Figure 55. Drift during slow tension test.

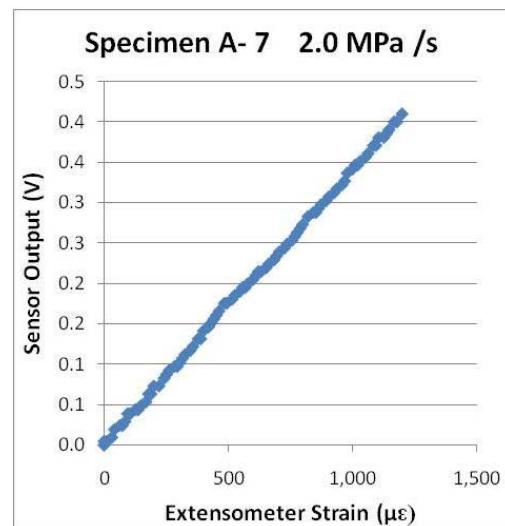


Figure 56. Minimal drift during fast tension test.

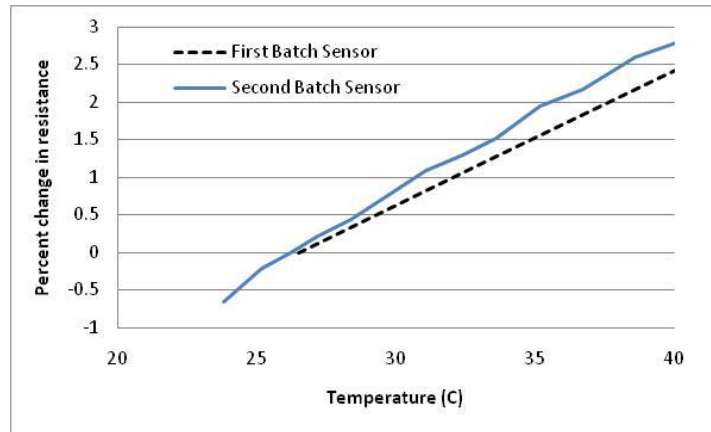


Figure 57. *Fuzzy fiber sensor thermal response.*

Fuzzy fibers were studied as strain sensors in the form of individual fibers, tows, monocomposites, and multi-layer composites. A test methodology was developed which included mechanical test parameters, instrumentation, and data acquisition. Specimen configurations were developed to characterize specific properties of the sensors. These included evaluating the sensor's longitudinal, transverse, and off-axis response, as well as the behavior near a stress concentration. Sensors imbedded longitudinally in straight-sided specimens were shown to demonstrate strain sensitivity. Studies using an open-hole stress-concentration specimen produced strain sensitivity, but did not detect the stress concentration due to the integration effect of the sensor length. Through the use of a specimen to study Poisson's effects, the sensors imbedded in the orthotropic layup specimen showed the expected response to transverse strain, while the unidirectional layup specimen had an unexpected reversal in polarity of the strain response. Further evaluation of the sensor behavior to off-axis loading with the "Star specimen" resulted in the demonstration of sensitivity to longitudinal, off-axis, and transverse strain. It was noted from this study that the fuzzy-fiber strain sensor has a gage factor in the 1-3 range, similar to metal foil strain gages.

Section 4

Oxidation Sensing

4.1 Use of the Fuzzy Fiber as an Oxidation Sensor

4.1.1 Objectives

The objective of this study was to develop and characterize CNT fuzzy fiber tows with sensing functions for the epoxy- and polyamides-based composites oxidation. The effort will focus on individual sensor development, incorporation into structural epoxy, and MVK14-based composites for the determination of degradation rate as function of time and, eventually, depict the oxidation mechanisms of those two matrices,

4.1.2 CNT Growth on Glass Fibers

CNT growth on glass fibers (labeled CNT fuzzy glass) was carried out using traditional chemical vapor deposition process. Two sets of fuzzy glass were prepared by changing only the growth time. CNT fuzzy glass with short resident time exhibits less-dense CNT growth than long resident time (Figures 58 and 59).

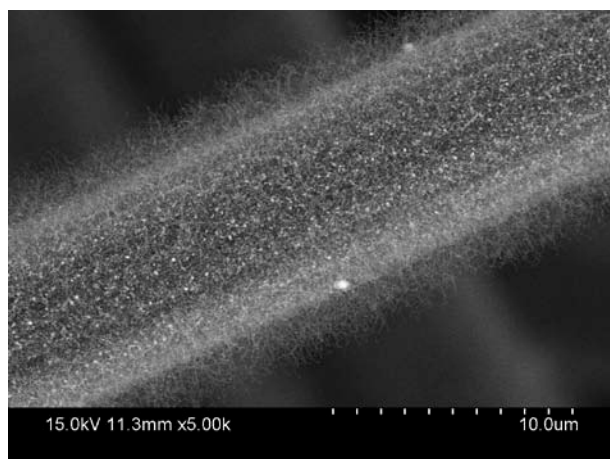


Figure 58. *Fuzzy fiber with less-dense CNT.*

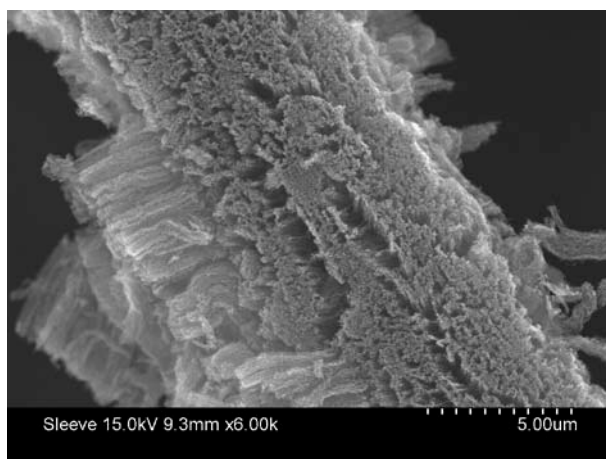


Figure 59. *Fuzzy fiber with very dense and longer CNT.*

4.1.3 Oxidation of Bare Fibers

Initially, these two sets of CNT fuzzy fibers were tested at 300° C in oxidative air environment. The experiment was carried out in a thermo-gravimetric analysis (TGA) chamber. The CNT fuzzy fibers were laid out and attached to copper wire leads using silver epoxy. The copper leads were attached to the data acquisition system, which was then connected to a laptop using Excelinx to record the data. The laptop recorded the resistance of all four sensors and temperature every 45 seconds. As shown in Figures 60 and 61, a small weight loss in the sample correspond to a drastic increase in electrical resistance. This change could be related either to the disruption in the electrical contact adjacent the CNTs or formation of any dielectric layer that may result in the carbon transformation from semi-crystalline to amorphous or adsorption of dielectric functional groups.

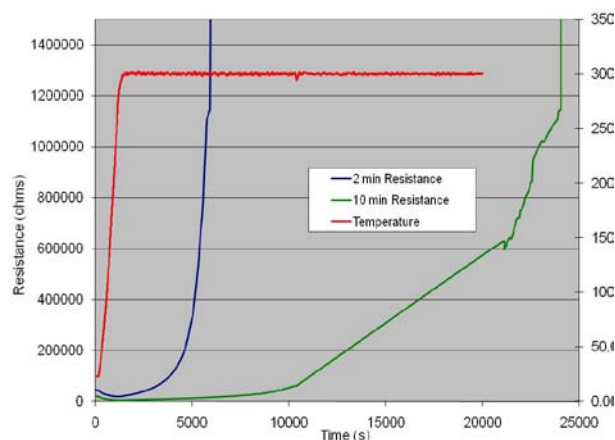


Figure 60. Resistance measurement of fuzzy fibers with 2- and 5-min. growth resident time.

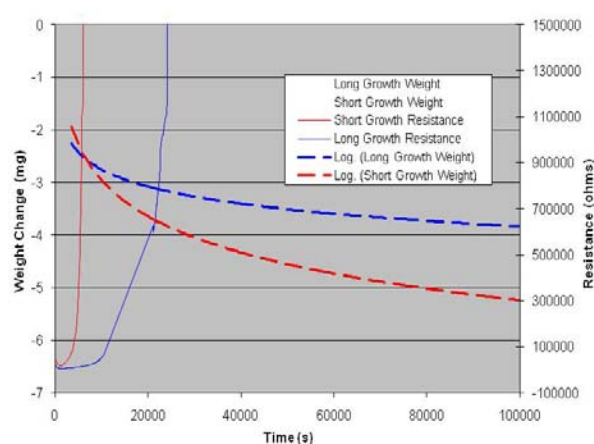


Figure 61. Weight loss and resistance measurement of fuzzy fibers with 2- and 5-min. growth resident time.

Since the ultimate goal is to use the CNT fuzzy glass as an oxidation sensor for BMI-based composites and these composites are supposed to sustain a maximum temperature of 280 C, we have decided to carry out additional experiments on new sets of CNT fuzzy fibers at lower temperature (about 280° C) using another experimental setup in which forced air could be adjusted (Figure 62). As shown in Figure 63, CNT fuzzy fiber is sensitive to any change in temperature fluctuation and behaves like a thermocouple. It is very well known that the resistance of carbon-based materials is dependent on temperature. Once the temperature is stable, the CNT fuzzy fiber is stable as well (Figures 63 and 64). A second run was carried out which shows the oxidation rate is fairly constant after using pre-conditioned fuzzy fibers to remove all kinds of adsorped liquids on the surface, such as humidity (Figures 65 and 66).

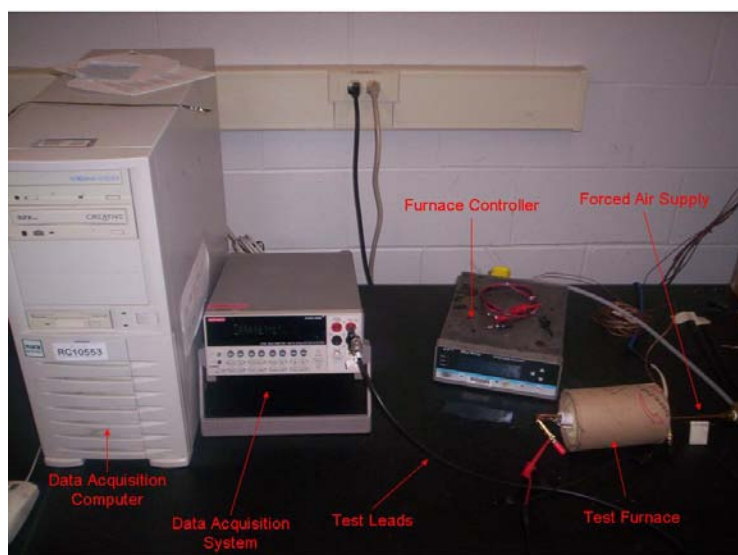


Figure 62. Resistance measurement setup.

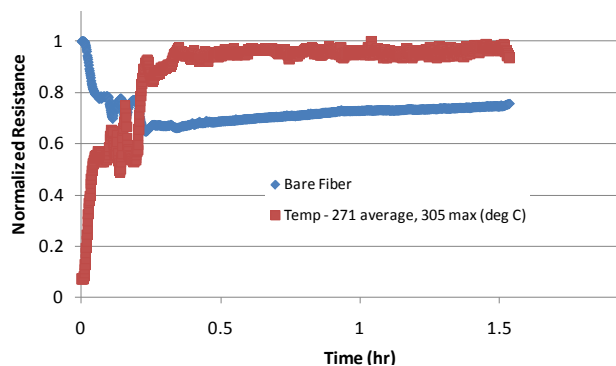


Figure 63. Resistance measurement of bare fuzzy fibers at average temperature.

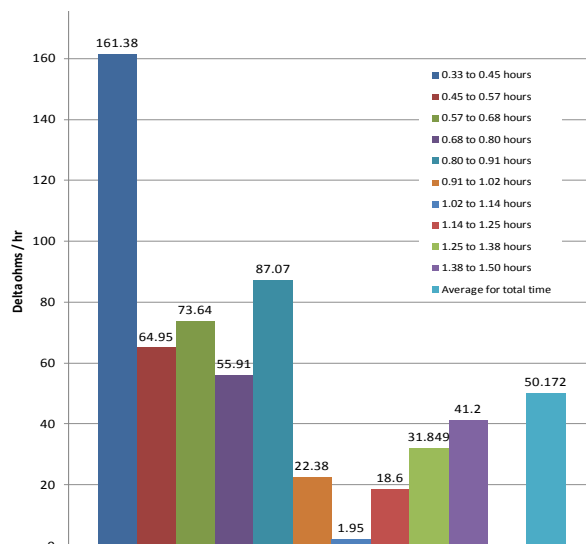


Figure 64. Oxidation rate measurement based on Figure 63.

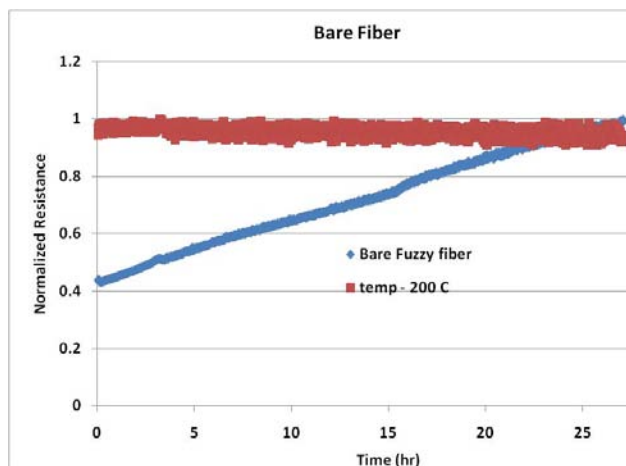


Figure 65. Resistance measurement of bare fuzzy fibers (second run).

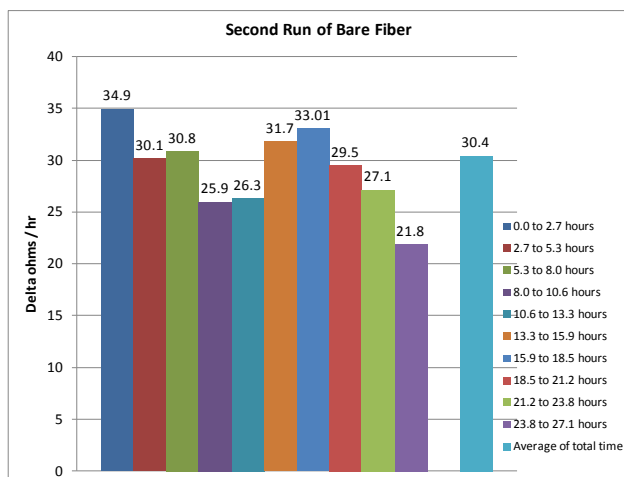


Figure 66. Oxidation rate measurement based on Figure 65.

To understand the sensing mechanism behind the increase in resistance, samples were subjected to various oxidation times and then their chemical composition examined by XPS. As shown in Figures 67 and 68, as time of oxidation increased, the amount of oxygen increases. The ratio O1s/C1s increased approximately by a factor of 10, from 10 min to 2 hours oxidation, and then remained constant after 5 hours oxidation time. After depicting the XPS pictures (Figure 69), it seems the relative amount of carbon bonded to oxygen-containing functions increased, indicating that oxygen chemically adsorbed to form either carboxylic, ether, or phenyl groups (Table 4). The fact that both carbon oxygen bonds (C-O) and carbonyl (C=O) have increased as the oxidation increases suggests a formation of carboxylic acid. Further investigation would be necessary to verify specifically which oxygen functional groups were predominant and was beyond the scope of this work.

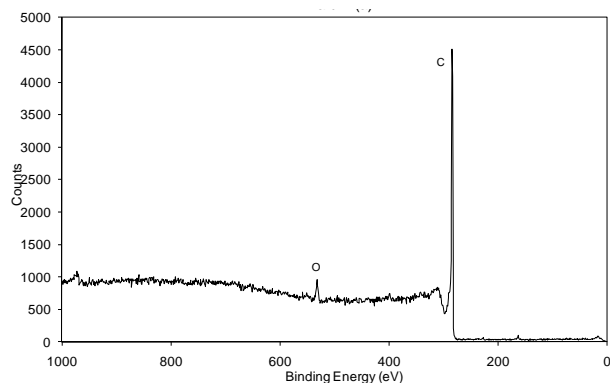


Figure 67. XPS of a sample oxidized for 30 min.

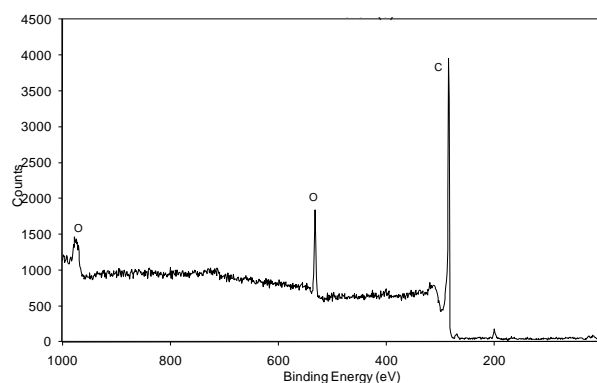


Figure 68. XPS of a sample oxidized for 5 hours.

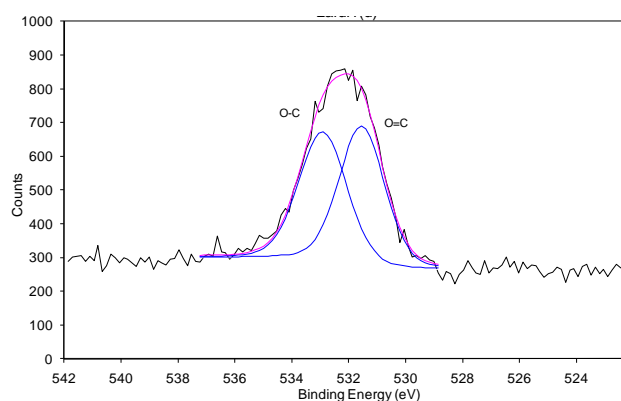


Figure 69. XPS zoom of the carbon oxygen picture for 5 hours oxidation's sample.

Table 4. XPS Results of Oxidized Samples Showing the Oxygen/Carbon Ratio

Oxidation Time	XPS - O 1s/C1s
30min	0.01
1 hour	0.08
2 hours	0.11
5 hours	0.14
10 hours	0.14

4.2 Use of CNT Fuzzy Fiber as an Oxidation Sensor in Epoxy-Based Composites

Composites were made and tested to see if CNT fuzzy fibers could be used to detect the oxidation of epoxy composites. The first step in making the composites was to make the sensors from CNT fuzzy fibers fibers. The CNT fuzzy fibers were laid out and attached to copper wire leads using silver epoxy (Figure 70). Once the sensors were ready, the composite was made by placing two layers of fiberglass on the top and bottom of two sensors with one layer of epoxy on each layer of fiberglass. Two more sensors were then placed on the top of the composite and it was then vacuum bagged and placed in the autoclave to cure. Figure 70 shows a sketch of the composites with each layer expanded.

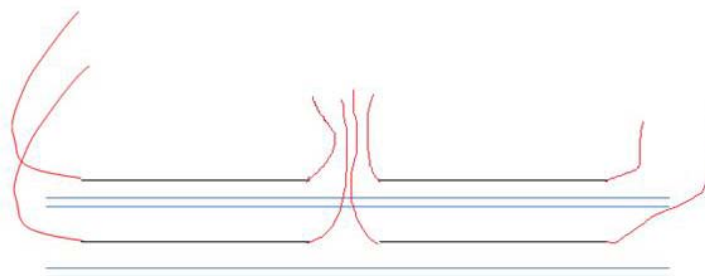


Figure 70. Expanded view of oxidation sensor composite. Blue lines are layers of fiberglass, black lines are hybrid fiber sensors. red lines are copper leads for the sensors.

The test setup consisted of a Keithley data acquisition system, heater, heater control, and computer. The test composite was placed in the heater such that two of the sensors were inside the heater and two were outside. The copper leads, as well as a thermal couple attached to the center of the part of the composite that was in the heater, were attached to the data acquisition system. The data acquisition was connected to the computer which used Excelinx to record the data. The computer recorded the resistance of all four sensors and temperature every 45 seconds. Figure 71 shows a rough sketch of the test setup.

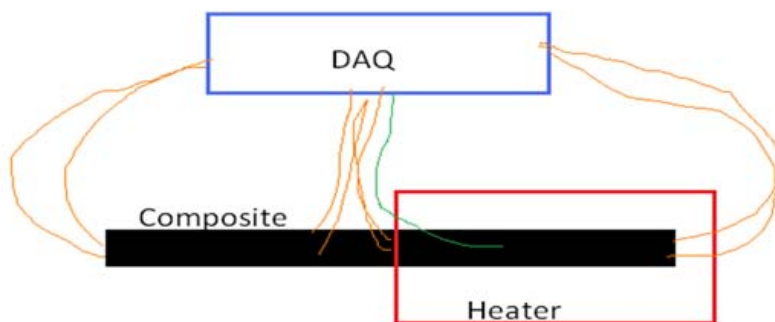


Figure 71. Sketch of test setup. Orange lines are copper wire leads attached to the data acquisition to measure resistance and the green line is the wire for the thermal couple on the surface of the composite connected to the data acquisition.

The average temperature recorded by the thermal couple on the composite inside the heater was 200° C. The one that was outside of the heater recorded an average temperature of 24.3° C. Figure 72 is a plot of the normalized resistance versus time of the two sensors inside the heater and Figure 73 is a plot of the two sensors outside of the heater.

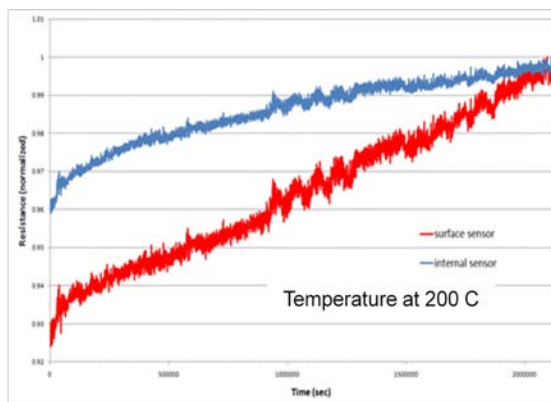


Figure 72. Resistance data for sensors inside of heater.

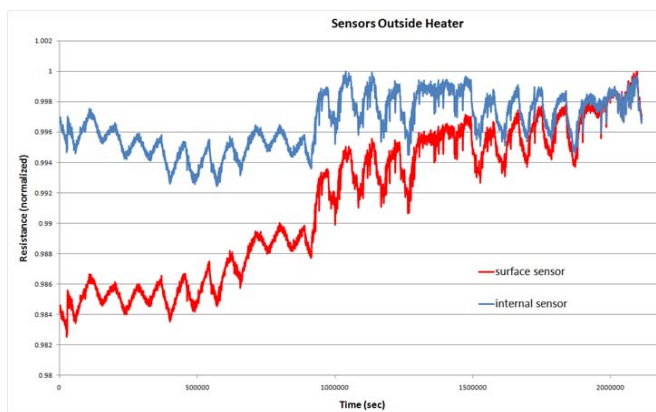


Figure 73. Data for sensors outside of heater.

These plots show that, over time in an oxidizing environment, the resistance of both of the sensors inside the heater increased. Furthermore, the sensor on the surface had a much-larger increase in resistance than the internal sensor. This makes sense, since the internal sensor was being protected by two layers of fiberglass on each side. On the other hand, there is not nearly as much increase in resistance if the sensors are not in an oxidizing environment. As the plot shows, the internal sensor outside the heater had almost no increase in resistance and, actually, decreased for a while. The surface sensor did have some increase in resistance, but not as much as the ones inside the heater.

For both sets of sensors (inside and outside of the heater), the surface sensor showed a bigger change in resistance over time than the internal sensors. This makes sense because they were on the surface and, therefore, did not have as much protection from the effects of their environment.

The plots in Figures 72 and 73 were used to determine the oxidation rate of the four sensors. This was accomplished by using a linear fit trendline on each of the plots, which gave an overall average. Each plot was then broken into ten segments to see how the oxidation rate changed during the test. The oxidation rates are presented in bar graph format in Figures 74 and 75.

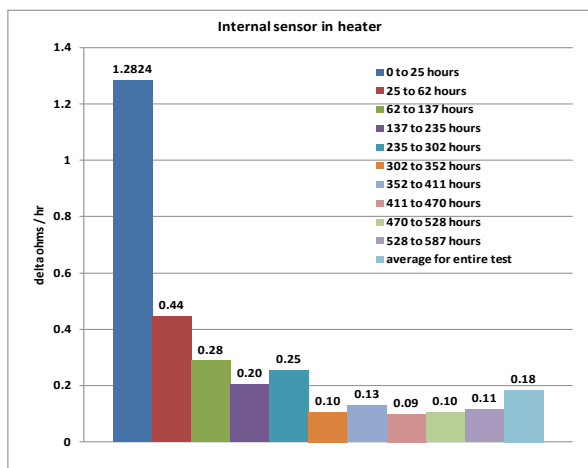


Figure 74. Oxidation rates for internal sensor inside heater.

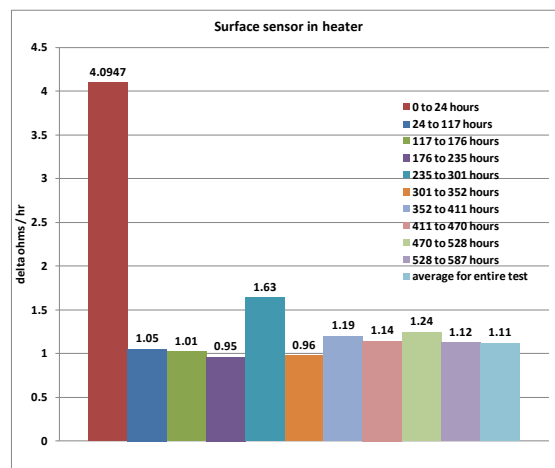


Figure 75. Oxidation rates for surface sensor inside heater.

The graphs for the sensors inside the heater both show an initial higher oxidation rate that lessens and levels out as time progresses. The graphs for the sensors outside of the heater are much more sporadic with negligible oxidation rate. Based on the data from this test, CNT fuzzy fibers can be successfully used as oxidation sensors in composites. Additional experiments were carried out to verify if these results are consistent and reproducible. It was confirmed that both surface and internal composites show the same behavior (Figures 76 and 77). As the oxidation time progressed, its rate diminished drastically, however, the oxidation is much higher on the exposed surface than inside the composite.

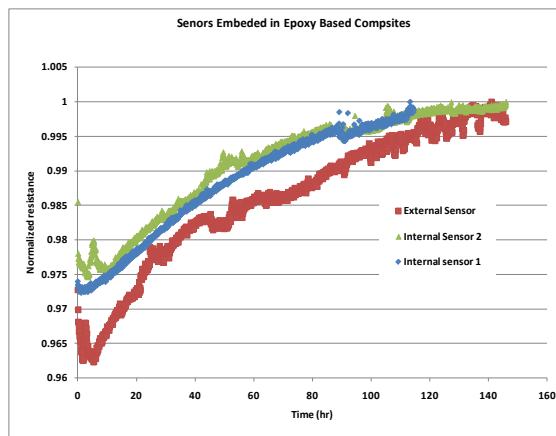


Figure 76. Data for epoxy-based composites (sensors outside of heater).

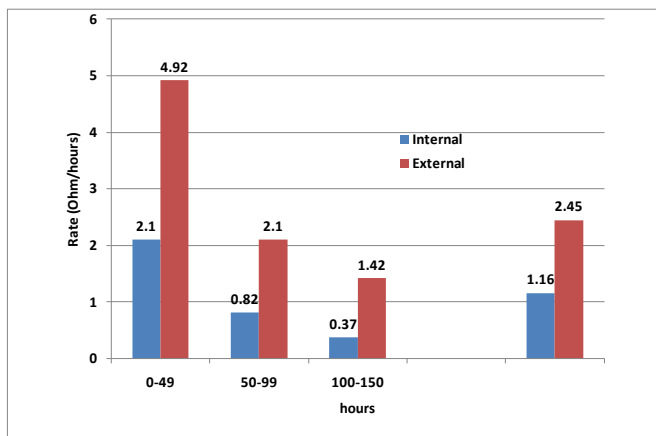


Figure 77. Oxidation rate comparison between external and internal sensor.

4.3 Use of CNT Fuzzy Fiber as Oxidation Sensor in MVK14-Based Composites

Polyimide-based composites were made using MVK14 matrix and the same layout of fibers as in epoxy-based composites. The oxidation temperature was about 288° C. The sample was subjected to natural air convection. After 450 hours, the oxidation seemed to occur only on the surface of the sample. As usual, the oxidation was very severe at the beginning and became very constant over time, to reach a steady-state condition. No measureable oxidation was observed on the internal sample (Figures 78 and 79). Additional experiments were carried out and lead to the same conclusions. As shown by SEM images, during oxidation, we had both development of small pits and cracks (Figures 80 and 81). It might be possible that, initially, pits are formed and, at some critical concentration, the matrix fails by development of cracks.

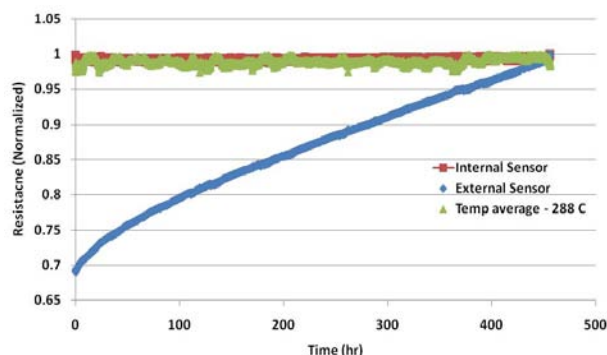


Figure 78. Data for MVK14-based composites.

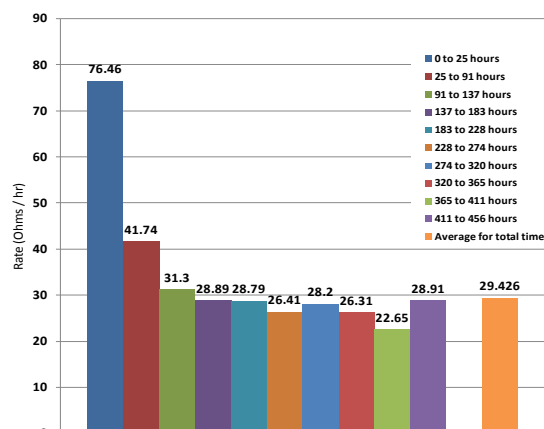


Figure 79. Oxidation rates for surface sensor for MVK14-based composites.

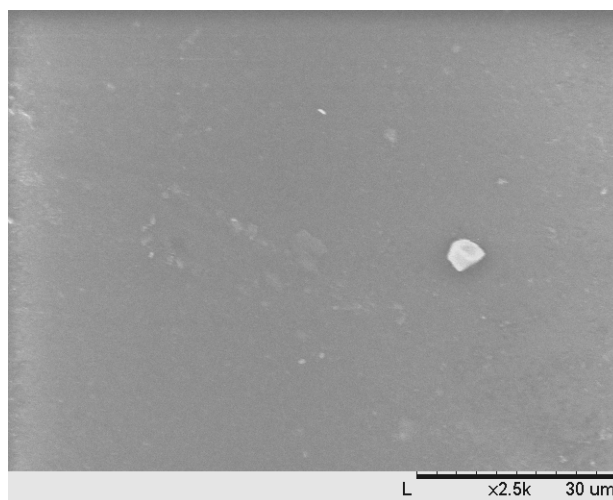


Figure 80. Pristine sample before oxidation.

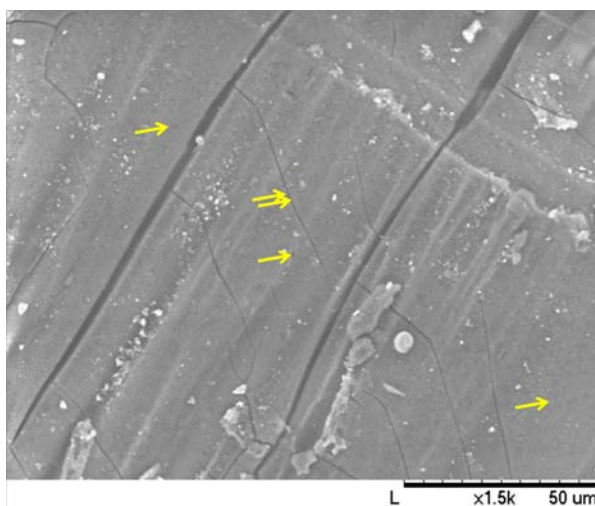


Figure 81. Sample after oxidation showing development of pits (single arrows) and cracks (double arrows).

4.4 Summary

As advanced fiber composites are utilized more frequently in primary structural applications, there is a key challenge to enhance the performance and reliability while reducing maintenance. As a consequence, there is tremendous scientific and technical interest in the development of techniques for monitoring the health of composite structures where real-time sensing can provide information on the state of chemistry and micro-structural damage. In this study, it has been established that carbon nanotubes grown on carbon or glass fiber (nicknamed fuzzy fibers) can be utilized as electrical networks by transforming the insulating glass fiber to very conductive one. The fuzzy fiber was inserted into traditional composites during layup operations and then used as *in situ* sensors for detecting changes during oxidation of advanced fiber composites. In order to gain an insight toward the oxidation rate and durability of polymer composites, the integration of electrical resistance measurements through fuzzy fiber ends was used as function time. Fuzzy fiber grids built into composites enables tracking of oxidation rates between oxidation occurring at the core and skin of the composites. Using spectroscopy techniques, we were able to depict the oxidation mechanism and oxidation rate. During the degradation process, first oxygen adsorption took place and then, as the oxidation phenomena progressed, pits and cracks developed that led into structural properties. We identified a parameter that may be utilized as a quantitative measure of oxidation rate.

4.5 Recommendation

All of the studies described above were carried out using natural convection. It will be very important to test these samples in a forced-air environment with changing humidity levels. It will also be crucial to know at what level of oxidation the structure of composites is affected.

Section 5

References

1. D.A. Jones, "Principles and Prevention of Corrosion", Prentice Hall, Upper Saddle River, NJ (1996).
2. X.H. Chen, C.S. Chen, H.N. Xiao, F.Q. Cheng, G. Zhang, and G.J. Yi, *Surface & Coatings Technology*, **191**, 351 (2005).
3. ASTM B117, "Standard Test Method of Salt Spray (Fog) Testing", ASTM International, 100 Barr Harbor Drive, PO Box C700, West Conshohocken, PA, 19428-2959 USA.
4. GM9540P, "Accelerated Corrosion Test", General Motors Engineering Standards, Detroit, MI, USA.
5. Andrews, J., A. Palazotto, M. DeSimio, and S. Olson, "Lamb Wave Propagation in Varying Isothermal Environments", accepted March 2008 for publication in *Structural Health Monitoring* (2008).
6. Olson, S., M. DeSimio, K. Brown, and M. Derriso, "Impact Localization in a Composite Wing Structure," proceedings of the Sensor, Signal and Information Processing workshop, Sedona, Arizona, May 2008.
7. Schulte, *et al*, "Load and Failure Analyses of CFRP Laminates by Means of Electrical Resistivity Measurement", *Composite Sci Technology*, 63; pp. 63-76 (1989).
8. Muto N., *et al.*, "Design of Intelligent Materials with Diagnosing Function for Preventing Fatal Fracture", *Smart Mater. Struct.*, **1**,1929-1934 (1992).
9. Arai Y., *et al.*, "Measurement of Electrical Conductivity and Detection of Water in Concrete with CFGFRP Used as Electrodes", *J. Ceram. Soc. Japan*, 102(12); pp. 745-51 (1994).
10. M. Pumera, S. Sanchez, I. Ichinose, and J. Tang, "Electrochemical Nanobiosensors", *Sens. Actuators B* 123, pp. 1195-1205 (2007).
11. K. Balasubramanian and M. Burghard, "Biosensors Based on Carbon Nanotubes", *Anal. Bioanal. Chem.* 385, pp. 452-468 (2006).
12. J. Wang, "Carbon-Nanotube Based Electrochemical Biosensors", *Electroanalysis* 17, pp. 7-14 (2005).
13. J.J. Gooding, "Nanostructuring Electrodes with Carbon Nanotubes: A Review on Electrochemistry and Applications for Sensing", *Electrochem. Acta* 50, pp. 3049-3060 (2005)
14. J. Wang, "Carbon-Nanotube Based Electrochemical Biosensors", *Electroanalysis* 17, p. 7 (2005).
15. L. Agui, P., Yanez-Sedeno, and J. M. Pingarron, *Anal. Chim. Acta* 622, p. 11, (2008).
16. M. Pumera, S. Sanchez, I. Ichinose, and J. Tang, *Sens. Actuators B* 123, p. 1195 (2007).
17. K. Balasubramanian and M. Burghard, *Anal. Bioanal. Chem.* 385, p. 452 (2006).
18. M. Trojanowicz, *Trends Anal. Chem.* 25, p. 480 (2006).
19. Y. Sun and H.H. Wang, *Appl. Phys. Lett.* 90, p. 213107 (2007).
20. Y. X. Liang, Y. J. Chen, and T. H. Wang, *Appl. Phys. Lett.* 85, p. 666 (2004).
21. P. Qi, O. Vermesh, M. Grecu, A. Javey, Q. Wang, H. Dai, S. Peng, and K.J. Cho, *Nano Lett.* 3, p. 347 (2003).
22. E. Bekyarova, M. Davis, T. Burch, M. E. Itkis, B. Zhao, S. Sunshine, and R. C. Haddon, *J. Phys. Chem. B* 108, p. 19717 (2004).
23. H.-M. So, K. Won, Y.H. Kim, B.-K. Kim, B.H. Ryu, P.S. Na, H. Kim, and J.-O. Lee, *J. Am. Chem. Soc.* 127, p. 11906 (2005).
24. C. Li, E.T. Thostenson, and T.-W. Chou, *Comp. Sci. Techn.* 68, p. 1227 (2008) .

25. C. Hierold, A. Jungen, C. Stampfer, and T. Helbling, *Sens. Actuators A* 136, p. 51 (2007).
26. E.T. Thostenson and T.-W. Chou, *Adv. Mater.* 18, p. 2837 (2006).
27. A.H. Barber, Q. Zhao, H.D. Wagner, and C.A. Baillie, *Comp. Sci. Techn.* 64, p. 1915 (2004).
28. P. Dharap, Z. Li, S. Nagarajaiah, and E.V. Barrera, *Sensor Review*, 24, p. 271 (2004).
29. C. Li and T.-W. Chou, *J. Intell. Mater. Sys. Struc.* 17, p. 247 (2006).
30. ASTM Standard D 5766/D 5766M, 2002a, "Standard Test Method for Open Hole Tensile Strength of Polymer Matrix Composite Laminate," ASTM International, West Conshohocken, PA, www.astm.org.
31. J.M. Whitney, I.M. Daniel, and R.B. Pipes, "Experimental Mechanics of Fiber Reinforced Composite Materials", Revised Edition, p. 49 (Brookfield Center, CT: Society for Experimental Mechanics, 1984).